Meso-scale Finite Element modeling of the Fracture Process Zone evolution for concrete

Yue Sun, Emmanuel Roubin, Jianfu Shao, Jean-Baptiste Colliat

Meso-scale Finite Element modeling of the Fracture Process Zone evolution for concrete

Yue SUN[a], Emmanuel ROUBIN[b], Jianfu SHAO[a] and Jean-Baptiste COLLIAT[a]

[a]Univ. Lille, CNRS, Centrale Lille, UMR 9013 - LaMcube - Laboratoire de Mécanique, Multiphysique, Multi-échelle, F-59000 Lille, France
[b]Université Grenoble Alpes, CNRS, Grenoble INP, 3SR, Grenoble F-38000, France

ARTICLE INFO

Keywords:
Meso-scale modeling
Fracture Process Zone
E-FEM method
Heterogeneous quasi-brittle material
Size effect of inclusions

ABSTRACT

The so-called Fracture Process Zone (FPZ) is well-known as a precursor of macroscopic failure for concrete. Moreover, it is a reasonable assumption that this FPZ extension is partly governed by the underlying random distribution of the material meso-structure. Therefore, meso-scale (millimeter scale) fracture simulations are effective in improving our understanding of this relationship. In this paper, our objective is to simulate the extension of cracks within the FPZ and to investigate the influence of spatial heterogeneity distribution. To this end, we propose to employ the Enhanced Finite Element Method (E-FEM) as our simulation tool. In the proposed simulation method, two types of discontinuities are incorporated within the elements: strong discontinuities serve to simulate actual cracks, while weak discontinuities allow for an explicit representation of heterogeneities. The combination of these two enhancements makes the model well-suited for investigating the FPZ at the meso-scale for being able to simulate complex crack features and interactions between cracks and aggregates. The simulation captures many crack patterns in the FPZ, such as diffused micro-cracks, macro-crack coalescence, multi-branching, and crack closures. The size effect of inclusions in the FPZ, which is widely observed in experiments, is also realized in simulations. The comparison with the experimental observations shows good consistency.

1. Introduction

It is a general consensus that the macroscopic failure behaviors of quasi-brittle materials, such as concrete and rocks, are strongly associated with the development of cracks at a fine scale. The formation of a macro-crack is a gradual process that begins with diffused micro-cracking and involves matrix-aggregate debonding, micro-crack coalescence (branching of cracks), and crack closures (Bažant and Pijaudier-Cabot, 1989; Wittmann and Hu, 1991; Mihashi and Nomura, 1996), see the sketch Fig. 1. This whole collection of mechanisms at the fine scale is dissipative and responsible for stress transfer. The subcritical zone that experiences micro-cracks is referred to as the Fracture Process Zone (FPZ), which can be observed in the vicinity and ahead of the macro-crack. Various experimental techniques have been developed to investigate the FPZ characteristics and track the crack propagation, such as Acoustic Emission (AE) measurements (Landis, 1999; Otsuka and Date, 2000; Muralidhara, Prasad, Eskandari and Karihaloo, 2010; Haidar, Pijaudier-Cabot, Dubé and Loukili, 2005), X-ray tomography techniques (Otsuka and Date, 2000; Landis, Nagy and Keane, 2003), and Digital Image Correlation techniques (Choi and Shah, 1997; Corr, Accardi, Graham-Brady and Shah, 2007; Tejchman et al., 2010; Wu, Rong, Zheng, Xu and Dong, 2011).

To numerically simulate the failure behaviors of material with cracking, multiple models have been proposed from a macroscopic point of view. In the concept of Representative Volume Element (RVE), the material can be considered as homogeneous. Under this hypothesis, various concepts that consider fracture mechanics have been proposed, such as the Linear elastic fracture mechanics (LEFM) (Griffith, 1921; Wells, 1961; Rice, 1968; Rice et al., 1968), the cohesive crack model (Dugdale, 1960; Barenblatt, 1962; Veselỳ and Frantík, 2014), the crack band theory (Bažant and Oh, 1983), and the cohesive zone model (Hillerborg, Modéer and Petersson, 1976), just mention a few.

These macro-scale models are robust and sophisticated for simulating various material behaviors. However, the definition of material parameters, such as fracture energy, is usually strongly related to the FPZ size, which is predominantly determined by the meso-structure of the material. Therefore, meso-scale models are proposed for a detailed analysis of the fracture process in the FPZ. Meso-scale models can be briefly divided into three categories based on their treatment of the displacement field: i) Continuum models: the displacement field is assumed to be continuous;

ORCID(s):

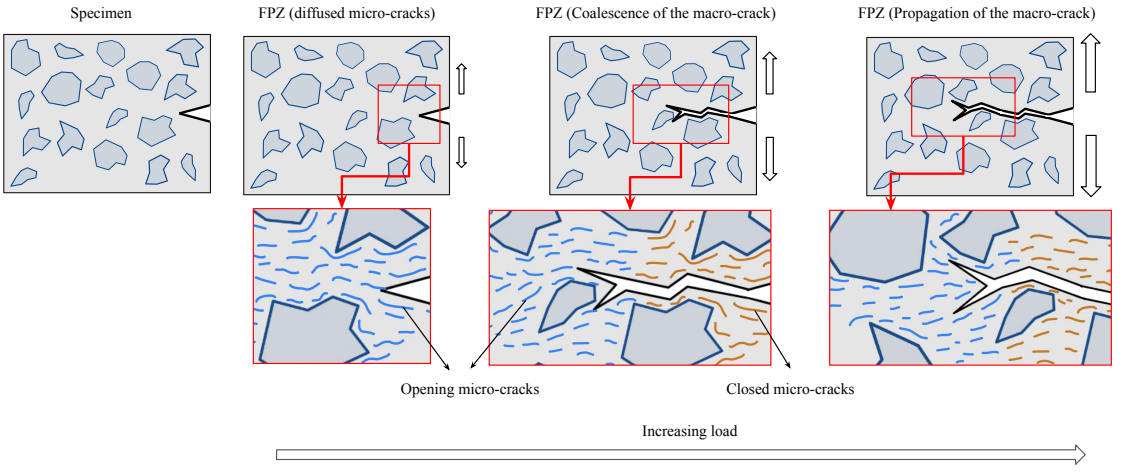

Figure 1: Concept of the crack evolution in the FPZ for heterogeneous media.

ii) Discrete models: the displacement field is considered to be established by rigid body motion of discrete units; iii) Discontinuous models: discontinuity is introduced into the displacement field.

For continuum models, one can incorporate the meso-structure directly into the finite element framework using randomly placed aggregates (Rodrigues, Manzoli and Bitencourt Jr, 2020; Zhou, Song and Lu, 2017; Tejchman et al., 2010), random fields (Georgioudakis, Stefanou and Papadrakakis, 2014; Vořechovskỳ and Sadílek, 2008), or X-ray tomography images. The latter technique makes it possible to incorporate real meso-structure into the finite element framework (Trawiński, Tejchman and Bobiński, 2018; Huang, Yang, Ren, Liu and Zhang, 2015). In some of these models, one layer of cement-aggregate interface element is used to simulate the Interfacial Transition Zone (ITZ). The mechanical behavior of the material can be simulated using damage-based constitutive models (Zhou and Chen, 2019; Rodrigues et al., 2020), plasticity theory (Zhang, Chen, Wang, Zhang, Wang and Li, 2019), or phase-field models (Nguyen, Yvonnet, Zhu, Bornert and Chateau, 2015). However, using the classical finite element method usually requires a conforming mesh strategy, which can lead to high computational costs and a limitation that cracks can only propagate along element boundaries. As a result, the crack trajectory is strongly influenced by the mesh alignment (Tijssens, Sluys and van der Giessen, 2000; Bažant and Jirásek, 2002; Zhou and Molinari, 2004).

Multiple discrete models have been proposed to investigate material fracture behavior at the meso-scale. The simplest of these is lattice models (Luković, Šavija, Schlangen, Ye and Van Breugel, 2016; Pan, Prado, Porras, Hafez and Bolander, 2017; Pan, Ma, Wang and Chen, 2018), where rigid aggregates can ideally be implemented using lattice elements. The heterogeneous meso-structure of the material can be obtained by using the X-ray scan images (Nitka, Tejchman et al., 2015), or by proposing spacial variations of material parameters, such as the tensile strength and fracture energy (Grassl and Bažant, 2009; Eliáš, Vořechovskỳ, Skoček and Bažant, 2015; Xenos, Grégoire, Morel and Grassl, 2015). Recent studies have aimed to simulate the Fracture Process Zone (FPZ) in concrete materials (Grassl, Grégoire, Solano and Pijaudier-Cabot, 2012; Grassl and Jirásek, 2010). The methodology employed in these studies is similar to the one used in the current work, where a heterogeneous meso-structure is generated through the placement of randomly distributed spherical aggregates with a minimum inter-aggregate distance. The observed crack patterns in these studies and the present work show similarities, including the presence of diffused micro-cracks in front of and adjacent to the macro-crack, as well as crack closures.

In the context of discontinuous models, two main strategies can be found in the literature that are distinguished by their support of additional degree of freedom: nodal enrichment, such as eXtended Finite Element Method (X-FEM) (Kumar, Singh, Mishra, Ahmad, Rao and Kumar, 2018; Moës, Dolbow and Belytschko, 1999; Moës and Belytschko, 2002; Benvenuti and Tralli, 2012; Li, Abdel-Wahab, Demirci and Silberschmidt, 2014); and elemental enrichment, such as Enhanced Finite Element Method (E-FEM). The discontinuous model enables discontinuity in the displacement field, and thus can represent cracks explicitly. In order to numerically investigate the fracture process in the FPZ at the meso-scale, the method used in this study is an E-FEM model.

The E-FEM model has been selected for this study due to its simple yet effective way to model the heterogeneous

meso-structure, as well as its ability to represent complex crack features. The former character is related to the weak discontinuity (Ortiz, Leroy and Needleman, 1987; Sukumar, Chopp, Moës and Belytschko, 2001), which represents a discontinuity in the strain field. The use of the non-adapted mesh strategy allows the automatic and efficient construction of high-quality meshes (Moës, Cloirec, Cartraud and Remacle, 2003). The latter character is associated with the strong discontinuity (Simo, Oliver and Armero, 1993; Wells, 2001), which represents a discontinuity in the displacement field. The discontinuity in the E-FEM model is incorporated as an internal variable inside the element. In a 3D model, the fracture energy is dissipated on a 2D discontinuity surface, rather than the entire 3D finite element volume, leading to mesh-size independence. Additionally, the weak and strong discontinuity are considered to be independent and additive (Benkemoun, Hautefeuille, Colliat and Ibrahimbegovic, 2010). The integration of both discontinuities allows for the simulation of complex crack features, including spontaneous crack initiation and multi-branching, as well as crack-aggregate interactions, such as debonding on the heterogeneity interface.

The structure of this paper is composed of six sections. After the introduction in the first section, Section 2 provides a kinematic description of the weak and strong enhancements. Then Section 3 concentrates on the mechanical behavior of the model at the local scale, where a mode-I crack opening-closing E-FEM model (Sun, Roubin, Shao and Colliat, 2021) is selected to simulate the evolution of the FPZ in concrete. This section addresses the four main phases of cohesive behavior on the strong discontinuity. Next, Section 4 outlines the resolution strategy of the model within the finite element framework. Subsequently, in Section 5, the present numerical model is used to simulate a notched cube with different inclusion sizes, with material parameters selected to match the corresponding experimental results by Otsuka (Otsuka and Date, 2000). The focus is made on the crack feature evolution in the FPZ under different loading levels and the effect of the aggregate size. Finally, a brief conclusion and discussion are given in Section 6 to close the paper.

Nomenclature

$\boldsymbol{B}$	standard strain interpolation matrix
$\boldsymbol{d}$	nodal displacements
$\boldsymbol{\varepsilon}$	strain field
$\boldsymbol{H}_{\mathrm{w}}$	equivalent normal vector matrix
$\boldsymbol{K}$	stiffness matrix
$\boldsymbol{n}$	normal vector on the discontinuity surface
$\mathcal{S}_{\varepsilon}$	weak discontinuities such as heterogeneity interfaces
$\boldsymbol{\sigma}$	stress field
$\mathcal{S}_{u}$	strong discontinuities such as cracks and fractures
$\boldsymbol{T}$	traction vector on the discontinuity surface
$\boldsymbol{u}$	theoretical displacement field
$\boldsymbol{C}$	elastic stiffness matrix of the Hooke's law
$\delta_{\mathcal{S}_u}$	Dirac-delta distribution that centered at the discontinuity surface
$[\lvert\boldsymbol{\varepsilon}\rvert]$	jump in the strain field
$[\lvert\boldsymbol{u}\rvert]$	jump in the displacement field
$\mathcal{G}_{\mathrm{cl}}$	necessary energy for completely closing the crack
$\mathcal{G}_{\mathrm{op}}$	fracture energy, which represents the necessary energy to create a fully opened crack
$\mathcal{G}_{\mathrm{re}}$	residual fracture energy for re-opening the crack
$\hat{\boldsymbol{u}}$	arbitrary displacement field
$\mathcal{H}_{\mathcal{S}_u}$	Heaviside function that centered at the discontinuity surface
Ω	reference domain in 3D
Ω_e	discretized finite element
σ_{y}	critical tensile strength
$\tilde{\bullet}/\hat{\bullet}$	weak/strong discontinuity
φ_e	continuous arbitrary function which has null value at Ω^- and unit value at Ω^+
E	Young's module
V	volume
$\bullet^+/\bullet^-$	upper/lower part of the sub-domain Ω^+ and Ω^+

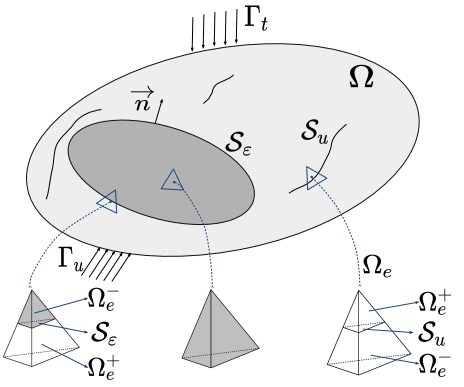

Figure 2: illustration of the solid that exhibiting heterogeneities and cracks, with their corresponding elements.

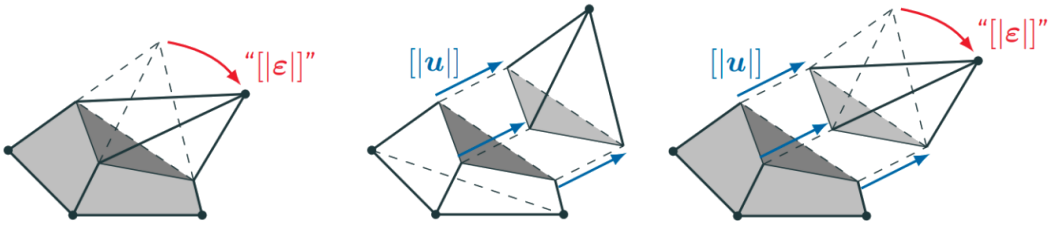

(a) Weak discontinuity (b) Strong discontinuity (c) Both weak and strong discontinuity

Figure 3: Three elements carrying different types of enhancements.

2. Kinematics enhancements at the meso-scale

This section starts by summarizing the basic notations that are employed in this paper. Then the kinematic descriptions and weak forms of the enhancements, the weak and strong discontinuities, are presented subsequently.

A sketch of the reference domain Ω is plotted in Fig. 2. It is a heterogeneous material which consists of a heterogeneity (dark gray part) and matrix (light gray part). By applying a non-adapted mesh strategy (Sukumar et al., 2001; Kamel, Colliat, Gerard and Massart, 2020), an unstructured mesh is projected to the heterogeneous material. Two kinds of enhancement are generated after the discretization:

- The weak discontinuity is embedded in the elements that are passed by the heterogeneity interface $\mathcal{S}_\varepsilon$. It brings a jump in the strain field $[|\boldsymbol{\varepsilon}|]$ to the element because of the difference between the materials' elastic properties, see Fig. 3(a).
- The strong discontinuity is embedded in the elements that are cut by a crack $\mathcal{S}_u$. It brings a jump in the displacement field $[|\boldsymbol{u}|]$ to the element, see Fig. 3(b).

The both discontinuities are oriented. An local orthogonal basis $(\boldsymbol{n}, \boldsymbol{m}, \boldsymbol{t})$ is built based on the normal vector $\boldsymbol{n}$ on the discontinuity surface. In the case of a debonding at the heterogeneity interface, the weak and strong discontinuities are independent and can be merged to the same element, see Fig. 3(c). The strain field writes as (Benkemoun, Hautefeuille, Colliat and Ibrahimbegovic):

$$\boldsymbol{\varepsilon}(\boldsymbol{x}) := \nabla^{\text{sym}}\bar{\boldsymbol{u}}(\boldsymbol{x}) + \tilde{\boldsymbol{\varepsilon}}(\boldsymbol{x}) + \hat{\boldsymbol{\varepsilon}}(\boldsymbol{x}), \tag{1}$$

where $\nabla^{\text{sym}} := \frac{1}{2}[\nabla(\bullet) + \nabla^T(\bullet)]$ is the symmetric gradient operator and $\bar{\boldsymbol{u}}$ is the regular part of the displacement field. Notation $\tilde{\bullet}$ / $\hat{\bullet}$ presents the weak / strong discontinuity, respectively.

2.1. Kinematic description and weak form of the weak discontinuity

As presented previously, the weakly enhanced elements are located at the heterogeneity interfaces of the material. The normal vector of the discontinuity interface $\boldsymbol{n}$ and the corresponding local basis $(\boldsymbol{n}, \boldsymbol{m}, \boldsymbol{t})$ is defined by the time of the

mesh projection. Since the displacement field is continuous across the discontinuity surface, the magnitude of the jump in the strain field $[|\boldsymbol{\varepsilon}|]$ can be entirely defined by three unknown values $\{[\varepsilon]_n, [\varepsilon]_m, [\varepsilon]_t\}^{\mathrm{T}}$ (Roubin, Vallade, Benkemoun and Colliat, 2015). The weakly enhanced part of the displacement field $\tilde{\boldsymbol{u}}$ writes as (Gurtin, 1973; Ibrahimbegović and Markovič, 2003):

$$\tilde{\boldsymbol{u}}(\boldsymbol{x}) = \Theta \boldsymbol{n} \cdot (\boldsymbol{x} - \boldsymbol{\xi})([\varepsilon]_n \boldsymbol{n} + [\varepsilon]_m \boldsymbol{m} + [\varepsilon]_t \boldsymbol{t}) \text{ with } \Theta = \begin{cases} \Theta^+ & \forall x \in \Omega_e^+ \\ \Theta^- & \forall x \in \Omega_e^- \end{cases}, \tag{2}$$

where $\boldsymbol{\xi}$ represents the position of interface surface, $\boldsymbol{n} \cdot (\boldsymbol{x} - \boldsymbol{\xi})$ can be seen as a signed distance to the discontinuity surface, and Θ is a still undefined function whose explicit expression is given later.

Correspondingly, the enhanced strain field can be calculated by taking the symmetrical gradient of $\tilde{u}$:

$$\tilde{\boldsymbol{\varepsilon}} = \nabla^{\mathrm{sym}}(\tilde{\boldsymbol{u}}) = \Theta \left([\varepsilon]_n \boldsymbol{n} \otimes \boldsymbol{n} + \frac{[\varepsilon]_m}{2} (\boldsymbol{n} \otimes \boldsymbol{m})^{\mathrm{sym}} + \frac{[\varepsilon]_t}{2} (\boldsymbol{n} \otimes \boldsymbol{t})^{\mathrm{sym}} \right). \tag{3}$$

2.2. Kinematic description and weak form of the strong discontinuity

An element is strongly enhanced if it is crossed by a crack. In this case, a jump in the displacement field is embedded in the element, the kinematic description of which writes as (Oliver, 1996b):

$$\boldsymbol{u} = \hat{\boldsymbol{u}} + (\mathcal{H}_{S_u} - \varphi_e)[|\boldsymbol{u}|], \tag{4}$$

where the displacement field $\boldsymbol{u}$ is decomposed into a continuous part $\hat{\boldsymbol{u}}$ and a discontinuous part $(\mathcal{H}_{S_u} - \varphi_e)[|\boldsymbol{u}|]$. In this equation, $\mathcal{H}_{S_u}$ is the Heaviside function that centered at the discontinuity interface, and φ_e is a continuous arbitrary function which has null value in Ω_e^-, and unit value at Ω_e^+. The magnitude of the jump in the displacement field $[|\boldsymbol{u}|]$ is considered as a constant function over Ω_e. The corresponding strain field can be obtained by taking the symmetric gradient of the displacement field Eq. 4 (Simo and Oliver, 1994; Oliver, 2000):

$$\boldsymbol{\varepsilon} = \nabla^{\mathrm{sym}} \boldsymbol{u} = \underbrace{\nabla^{\mathrm{sym}} \hat{\boldsymbol{u}}}_{\text{regular}} \underbrace{-([|\boldsymbol{u}|] \otimes \nabla \varphi_e)^{\mathrm{sym}}}_{\text{bounded enhancement } \hat{\varepsilon}_b} + \underbrace{\delta_{S_u}([|\boldsymbol{u}|] \otimes n)}_{\text{unbounded enhancement } \hat{\varepsilon}_u}. \tag{5}$$

The term δ_{S_u} is the Dirac-delta distribution which comes from the gradient of the Heaviside function.

3. Mechanical behaviors at the meso-scale

In this section, the focus is made on the mechanical behaviors of the model at the local scale, especially the fracture behaviors related to the cracks. As pointed out previously, cracks are presented by strong discontinuities in this model, namely the strong discontinuity analysis (Simo et al., 1993). It aims at ensuring the consistency of the model in the presence of a jump in the displacement field, which will result in an unbounded enhancement as presented in Eq. 5. In this paper, the *Discrete Strong Discontinuity Approach* (DSDA) (Oliver, 2000; Brancherie and Ibrahimbegovic, 2009; Kucerova, Brancherie, Ibrahimbegovic, Zeman and Bittnar, 2009) is used, which discretizes the strongly enhanced element into two parts:

- On the discontinuity interface, a traction vector $\boldsymbol{T}$ is presented, which is continuous and serves as a bright linking the two sub-volumes through the discontinuity surface.
- Beyond the discontinuity interface, the bulk volumes is pure elastic and can be fully described by the Hooke's law.

In this framework, the nonlinear behaviors are entirely concentrated on the discontinuity. The governing law of these behaviors is depicted by a relationship between the traction vector $\boldsymbol{T}$ and the crack opening $[|\boldsymbol{u}|]$, namely the *traction-separation law* (Wells, 2001; Dias-da Costa, Alfaiate, Sluys and Júlio, 2009a,b). In existing E-FEM models, several types of cracking modes have been proposed and put into literature, such as the mode-I traction-opening model (Roubin et al., 2015; Sun et al., 2021), the mode-II sliding-opening model (Hauseux, Roubin, Seyedi and Colliat, 2016; Yue, Roubin, Jianfu and Colliat, 2021), and the mix-mode of the mode-I and mode-II is also under investigation (Laborin, Malecot, Roubin and Daudeville).

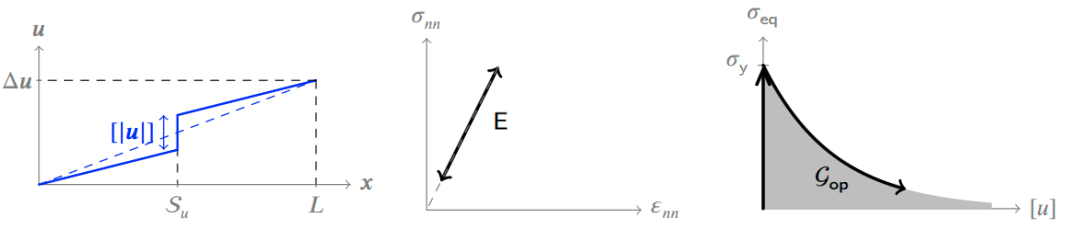

(a) Displacement field (b) Behavior outside the discontinuity (c) Behavior on the discontinuity

Figure 4: Behavior of the strongly enhanced element at the crack opening phase.

In this paper, considering that the mode-I crack mode is fairly a common choice for modeling FPZ, the mode-I model with the crack opening-closing mechanism (Sun et al., 2021) is selected. Hence, in the subsequent four parts of the section, the localization criterion, the opening law, and the closing law are presented. These governing laws describe the fracture behaviors of a quasi-brittle material at the local-scale.

3.1. Localization criterion

The localization criterion determines the moment of failure initiation and the orientation of the crack. It is a stress-based criterion which writes as:

$$\Phi_{\mathrm{l}} = \sigma_{\mathrm{eq}} - \sigma_{\mathrm{y}}, \tag{6}$$

where the equivalent stress σ_{eq} is compared with a critical value σ_{y} (local material property). A negative value of Φ_{l} means an elastic behavior while a positive value presents that the localization occurs in the element. Depending on the localization takes place in a homogeneous element or a heterogeneous element, two situations are considered:

- In the case of homogeneous element, the equivalent stress is defined as the major principal stress σ_I. Correspondingly, the crack orientation $\boldsymbol{n}$ is determined by the major eigenvector.
- In the case of heterogeneous element, where a weak discontinuity is already present in the element, we consider a hypothesis that the strong discontinuity takes place on the same surface (Ibrahimbegovic and Melnyk, 2007; Benkemoun et al., 2010). The equivalent stress is defined as the projection of traction vector on the pre-defined interface: $\sigma_{\mathrm{eq}} = \boldsymbol{T} \cdot \boldsymbol{n}$. This choice is made on the experimental observations that the cracks tend to appear at the interface between mortar and aggregates because the *Interfacial Transition Zone* (ITZ) (Scrivener, Crumbie and Laugesen, 2004; Jebli, Jamin, Malachanne, Garcia-Diaz and El Youssoufi, 2018) usually carries a higher porosity, which make it a weaker zone for concrete.

3.2. Traction-opening criterion

After the initiation of the crack, we consider a cohesive traction-opening procedure to the crack, see Fig. 4. As the crack opening value $[|\boldsymbol{u}|]$ increases, the cohesion linking the two bulk sub-volumes decreases. A classical softening criterion is used to depict this mechanical behavior at the discontinuity:

$$\Phi_{\mathrm{o}} = \sigma_{\mathrm{eq}} - \underbrace{\sigma_{\mathrm{y}} \exp\left(-\frac{\sigma_{\mathrm{y}}}{\mathcal{G}_{\mathrm{op}}}[u]\right)}_{q_{\mathrm{o}}}. \tag{7}$$

In this equation, two local material parameters are applied: the critical tensile stress σ_{y} and the fracture energy $\mathcal{G}_{\mathrm{op}}$ (the gray zone in Fig. 4). The latter parameter presents the necessary energy to completely open a crack of 1 m^2. Upon this consideration, a larger fracture energy $\mathcal{G}_{\mathrm{op}}$ presents a more ductile material behavior.

An analytical solution is available for the non-linear resolution of Eq. 7, readers can refer to section 4.2 for more details.

3.3. Closing criterion

In case of a non-proportional loading is applied to an element that carries a opened crack, the tensile stress on the discontinuity interface could reduce progressively or even turns to compression. For a model without closure mechanism, no energy can be dissipated in this phase since the opening value $[|\boldsymbol{u}|]$ remains constant, see Fig. 5(a). For a model with closure (Sun et al., 2021), on the other hand, permits the closing of the opened cracks and the energy dissipation. These are crucial ingredients for the failure behaviors of quasi-brittle materials under non monotonic loadings such as cyclic compression tests. The closing procedure includes several stages, see Fig. 5(b).

As the firs moment of the unloading, the discontinuity interface is still under tension. The first phase therefore corresponds to a decrease of the tensile stress on the discontinuity interface, see stage (1) to stage (2) in the figure. The opening value $[|\boldsymbol{u}|]$ will remain unchanged before a fully release of the elastic energy that is stored in the bulk volumes.

Subsequently, as the loading continue decreases, a compressive stress is applied to the discontinuity interface, and the closing criterion is triggered. We consider here an exponential form for the closing criterion. It leads to an increasing required compressive load to close the crack. It is impossible to completely close the crack, which means that the opened crack cannot be healed. Upon consideration, the closing criterion writes as:

$$\Phi_{\mathrm{c}} = -\sigma_{\mathrm{eq}} + \underbrace{\frac{\mathcal{G}_{\mathrm{cl}}}{[u]_{\max}} \ln\left(\frac{[u]}{[u]_{\max}}\right)}_{q_{\mathrm{c}}}, \tag{8}$$

where $\mathcal{G}_{\mathrm{cl}}$ is the necessary energy for completely closing the crack, and $[u]_{\max}$ is the largest opening value. Here, an assumption is adopted that the fracture energy for closing (light gray part in the left in Fig. 5(b)) equals to the consumed energy in opening (dark gray part in Fig. 5(b)): $\mathcal{G}_{\mathrm{cl}} := \mathcal{G}'_{\mathrm{op}}$. This part of the energy is calculated as:

$$\mathcal{G}'_{\mathrm{op}} = \int_0^{[u]_{\max}} \sigma_{\mathrm{eq}}([u])\, d[u] = \mathcal{G}_{\mathrm{op}}\left(1 - \exp\left(-\frac{\sigma_{\mathrm{y}}\,[u]_{\max}}{\mathcal{G}_{\mathrm{op}}}\right)\right) = \mathcal{G}_{\mathrm{cl}}. \tag{9}$$

This assumption makes a larger opened element more difficult to close completely. Furthermore, it saves us from adding additional material parameters.

3.4. Re-opening criterion

Let us now consider that the closed element is now reloaded. As presented in the closing phase, the first mechanical behaviors is pure elastic, see stage (3) to stage (4) in Fig. 5(c). The compressive stress on the discontinuity surface progressively decreases and the tensile stress increases until reaches the critical tensile stress. Then the re-opening criterion is triggered (stage (4) to stage (5)). In this model, it is considered that the already damaged element cannot completely recovered, even the crack is partially closed. The degradation of the element is permanent and irreversible. The re-opening criterion is calculated with the lowest residual tensile strength and the residual fracture energy $\mathcal{G}_{\mathrm{re}} = \mathcal{G}_{\mathrm{op}} - \mathcal{G}'_{\mathrm{op}}$. The re-opening criterion writes as:

$$\Phi_{\mathrm{o}} = \sigma_{\mathrm{eq}} - \sigma'_{\mathrm{y}}\left(1 - \exp\left(-\frac{\sigma'_{\mathrm{y}}}{\mathcal{G}_{\mathrm{re}}}[u]\right)\right), \text{ with } \begin{cases} \sigma'_{\mathrm{y}} & = \sigma_{\mathrm{y}} \exp\left(-\dfrac{\sigma_{\mathrm{y}}\left([u]_{\max} - [u]_{\mathrm{cl}}\right)}{\mathcal{G}_{\mathrm{op}}}\right) \\ \mathcal{G}_{\mathrm{re}} & = \mathcal{G}_{\mathrm{op}} \exp\left(-\dfrac{\sigma_{\mathrm{y}}\left([u]_{\max} - [u]_{\mathrm{cl}}\right)}{\mathcal{G}_{\mathrm{op}}}\right) \end{cases}. \tag{10}$$

4. Resolution scheme of the Finite Element framework with double enhancements

This section aims at presenting the resolution strategy of the E-FEM model. The main difficulty is focused on the treatment of the kinematic enhancements, especially the treatment of the unbounded part, such as the Dirac-delta distribution in the strain field that results from the strong discontinuity. In this paper, both strong and weak discontinuities $[|\boldsymbol{u}|]$ and $[|\boldsymbol{\varepsilon}|]$ are solved inside the element as additional unknown variables at the local scale. The unbounded

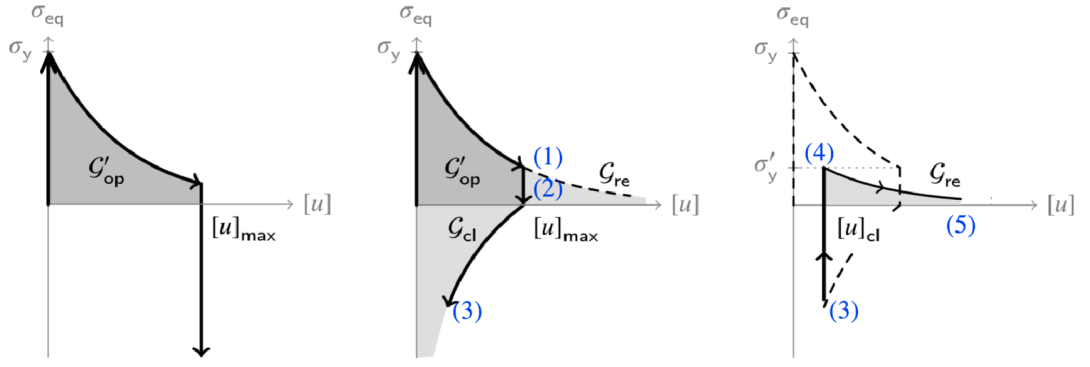

(a) Model without closure mechanism (b) Model with closure in the closing phase (c) Model with closure in the re-opening phase

Figure 5: Mechanical behavior of the local constitutive models at the discontinuity interface.

(incompatible) kinematics is solved in a compatible form by applying the Statically and Kinematically Optimal Non-symmetric Formulation (SKON) (Dvorkin, Cuitiño and Gioia, 1990; Simo and Oliver, 1994; Oliver, 1996a). It leads to a non-invasive form for the E-FEM model, which makes it possible to solve the system in a standard and classical Finite Element framework. Moreover, it allows the model to simulate multi-branching cracks, and the size of the solving system stays constant during the appearance of the new cracks.

Since the kinematic description of the weak and strong discontinuities has been documented many times in the literature (Roubin et al., 2015; Yue et al., 2021; Sun et al., 2021), the author choose to keep the writing as light as possible for the sake of reading. This section contains two parts. We show in the first part the discretization of the system. Then the resolution of the non-linear equation at the local scale is presented in the second part.

4.1. Discretization of the system

Depending on the element is in the opening procedure or the closing procedure, the linearized element can be written in a matrix form.

- If the element is opening:

$$\begin{bmatrix} \boldsymbol{K}_{bb} & \boldsymbol{K}_{bw} & \boldsymbol{K}_{bs} \\ \boldsymbol{K}_{wb} & \boldsymbol{K}_{ww} & \boldsymbol{K}_{ws} \\ \boldsymbol{K}_{s^*b} & \boldsymbol{K}_{s^*w} & \boldsymbol{K}_{s^*s} + K_{qo} \end{bmatrix}^{(k)}_{n+1} \begin{Bmatrix} \Delta \boldsymbol{d} \\ \Delta[|\varepsilon|] \\ \Delta[u] \end{Bmatrix}^{(k+1)}_{n+1} = \begin{Bmatrix} -(\boldsymbol{f}^e_{int} - \boldsymbol{f}^e_{ext}) \\ -\mathcal{R}^e_{[|\varepsilon|]} \\ -\Phi_o \end{Bmatrix}^{(k)}_{n+1}, \tag{11}$$

- If the element is closing:

$$\begin{bmatrix} \boldsymbol{K}_{bb} & \boldsymbol{K}_{bw} & \boldsymbol{K}_{bs} \\ \boldsymbol{K}_{wb} & \boldsymbol{K}_{ww} & \boldsymbol{K}_{ws} \\ -\boldsymbol{K}_{s^*b} & -\boldsymbol{K}_{s^*w} & -\boldsymbol{K}_{s^*s} + K_{qc} \end{bmatrix}^{(k)}_{n+1} \begin{Bmatrix} \Delta \boldsymbol{d} \\ \Delta[|\varepsilon|] \\ \Delta[u] \end{Bmatrix}^{(k+1)}_{n+1} = \begin{Bmatrix} -(\boldsymbol{f}^e_{int} - \boldsymbol{f}^e_{ext}) \\ -\mathcal{R}^e_{[|\varepsilon|]} \\ -\Phi_c \end{Bmatrix}^{(k)}_{n+1}, \tag{12}$$

where the subscript n presents the time step, and the superscript (k) denotes the resolution iteration step. The explicit expression of each matrix is given in the appendix.

In Eq. 11 and Eq. 12, the three incremental terms $\{\Delta \boldsymbol{d}, \Delta[|\varepsilon|], \Delta[u]\}$ are solved in two different levels. First, the weak and strong discontinuity $(\Delta[|\boldsymbol{\varepsilon}|]^{k+1}_{n+1}, \Delta[|\boldsymbol{u}|]^{k+1}_{n+1})$ are solved at the element level as internal variables for a fixed displacement field $\boldsymbol{d}^k_{n+1}$. It would lead to a null residual of $\mathcal{R}^e_{[|\boldsymbol{\varepsilon}|]}$ and balanced opening/closing criterion Φ_o/Φ_c. Then the displacement field can be solved at the global level by making a static condensation on the local variables (Wilson, 1974). The solving equation of the assembled global system writes as:

$$\mathbb{K}_{sc}\Big|^{(k)}_{n+1} \Delta \boldsymbol{d}\Big|^{(k+1)}_{n+1} = -\mathop{\mathbb{A}}_{e=1}^{n_e} \{\boldsymbol{f}^e_{int} - \boldsymbol{f}^e_{ext}\}\Big|^{(k)}_{n+1}, \text{with } \mathbb{K}_{sc}\Big|^{(k)}_{n+1} = \mathop{\mathbb{A}}_{e=1}^{n_e} \boldsymbol{K}_{sc}\Big|^{(k)}_{n+1}. \tag{13}$$

Providing that the local variables are now computed, the modified stiffness matrix $\boldsymbol{K}_{\mathrm{sc}}$ can be calculated by writing the internal variables in terms of the displacement:

- If the element is opening:

$$\boldsymbol{K}_{\mathrm{sc}}\Big|_{n+1}^{(k)} = \boldsymbol{K}_{\mathrm{bb}} - \begin{bmatrix}\boldsymbol{K}_{\mathrm{bw}} & \boldsymbol{K}_{\mathrm{bs}}\end{bmatrix}\left(\begin{bmatrix}\boldsymbol{K}_{\mathrm{ww}} & \boldsymbol{K}_{\mathrm{ws}} \\ \boldsymbol{K}_{\mathrm{s^*w}} & \boldsymbol{K}_{\mathrm{s^*s}} + K_{\mathrm{qo}}\end{bmatrix}_{n+1}^{(k)}\right)^{-1}\begin{bmatrix}\boldsymbol{K}_{\mathrm{wb}} \\ \boldsymbol{K}_{\mathrm{s^*b}}\end{bmatrix}_{n+1}^{(k)}, \tag{14}$$

- If the element is closing:

$$\boldsymbol{K}_{\mathrm{sc}}\Big|_{n+1}^{(k)} = \boldsymbol{K}_{\mathrm{bb}} - \begin{bmatrix}\boldsymbol{K}_{\mathrm{bw}} & \boldsymbol{K}_{\mathrm{bs}}\end{bmatrix}\left(\begin{bmatrix}\boldsymbol{K}_{\mathrm{ww}} & \boldsymbol{K}_{\mathrm{ws}} \\ -\boldsymbol{K}_{\mathrm{s^*w}} & -\boldsymbol{K}_{\mathrm{s^*s}} + K_{\mathrm{qc}}\end{bmatrix}_{n+1}^{(k)}\right)^{-1}\begin{bmatrix}\boldsymbol{K}_{\mathrm{wb}} \\ -\boldsymbol{K}_{\mathrm{s^*b}}\end{bmatrix}_{n+1}^{(k)}. \tag{15}$$

It can be seen from Eq. (14) and Eq. (15) that the modified stiffness matrix $\mathbb{K}_{\mathrm{sc}}$ has the same dimension as the elastic stiffness matrix $\mathbb{K}_{\mathrm{bb}}$. It confirms the non-invasive form of the E-FEM model that the enhancements will not increase the global unknowns of the solving system. However, the resolution of the non-linear equations of the strong discontinuity requires increasing computation time. Some analytical solutions are available for this problem which decrease significantly the computation time, they are presented subsequently.

4.2. Resolution of the local non-linear equations

It can be seen from Eq. 11 and Eq. 12 that the non-linearity of the system is only located at the resolution of the strong discontinuity, which is related to the non-linear crack opening/closing criterion Eq. 7 and Eq. 8. Being equations in terms of the crack opening value $[u]$, these two criteria can be reformulated into the following form:

- The crack opening criterion (Roubin et al., 2015):

$$T_e + M[u] = \sigma_{\mathrm{y}} \exp\left(-\frac{\sigma_{\mathrm{y}}}{\mathcal{G}_{\mathrm{op}}}[u]\right), \text{ with } \begin{cases} T_e &= \left(\boldsymbol{K}_{\mathrm{s^*b}} - \boldsymbol{K}_{\mathrm{s^*w}}\boldsymbol{K}_{\mathrm{ww}}^{-1}\boldsymbol{K}_{\mathrm{wb}}\right)\boldsymbol{d}, \\ M &= \left(\boldsymbol{K}_{\mathrm{s^*s}} - \boldsymbol{K}_{\mathrm{s^*w}}\boldsymbol{K}_{\mathrm{ww}}^{-1}\boldsymbol{K}_{\mathrm{ws}}\right). \end{cases} \tag{16}$$

- The crack closing criterion (Sun et al., 2021):

$$-T_e - M[u] = \frac{\mathcal{G}_{\mathrm{cl}}}{[u]_{\max}} \ln\left(\frac{[u]}{[u]_{\max}}\right). \tag{17}$$

The analytical solutions can be obtained by using the Lambert function W_0 (Corless, Gonnet, Hare, Jeffrey and Knuth, 1996). For the element in the opening procedure, the crack opening value $[u]$ is solved as:

$$[u] = \frac{\mathcal{G}_{\mathrm{op}}}{\sigma_{\mathrm{y}}}\left(W_0\left(\frac{\sigma_{\mathrm{y}}^2 \exp(\frac{\sigma_{\mathrm{y}} T_e}{\mathcal{G}_{\mathrm{op}} M})}{\mathcal{G}_{\mathrm{op}} M}\right) - \frac{\sigma_{\mathrm{y}} T_e}{\mathcal{G}_{\mathrm{op}} M}\right). \tag{18}$$

For the element in the closing phase, the analytical solution writes as:

$$[u] = -\mathcal{G}_{\mathrm{cl}} W_0\left(-\frac{M[u]_{\max}^2 \exp(\frac{T_e[u]_{\max}}{\mathcal{G}_{\mathrm{cl}}})}{\mathcal{G}_{\mathrm{cl}}}\right) \Big/ \left(M[u]_{\max}\right). \tag{19}$$

The weak discontinuity $[|\boldsymbol{\varepsilon}|]$ can be determined by the solution of $[|\boldsymbol{u}|]$, the expression gives as:

$$[|\varepsilon|] = -\boldsymbol{K}_{\mathrm{ww}}^{-1}\left(\boldsymbol{K}_{\mathrm{wb}}\boldsymbol{d} + \boldsymbol{K}_{\mathrm{ws}}[u]\right). \tag{20}$$

Therefore, all local non-linear equations are resolved and the internal unknown variables are determined. Then the assembled modified stiffness matrix $\mathbb{K}_{\mathrm{sc}}$ can be completely defined for the resolution of the global system. This model is implemented in a opened FE code FEAP (Taylor, 1987). The non-linear global system is solved by using a quasi-Newton BFGS algorithm (Matthies and Strang, 1979).

5. Meso-scale modeling of the FPZ in concrete - Noteched cube

As previously stated, research has demonstrated that the formation of macro-cracks can result from a complex process starting with the scattered micro-cracks in the Fracture Process Zone (FPZ) (Bažant and Oh, 1983). This section focuses on the investigation of this transition process from micro-cracks at the fine-scale to macro-cracks using an E-FEM model. The simulation is based on an experiment performed by Koji Otsuka in 2000 (Otsuka and Date, 2000). In this article, experiments are carried out with X-ray and Acoustic emission (AE) techniques to investigate the FPZ behavior in concrete. The effect of the aggregate size is also evaluated.

It is important to note that the numerical simulation has several limitations, which are addressed by making certain simplifications:

- The model resolution is static and does not consider the rate of loading.
- The volume fraction and granulometry of the aggregate in the concrete are not provided in the article, so we chose a volume fraction of 30% and an 'S-shaped' curve for the aggregate granulometry to adapt to a general case of concrete.
- The environmental influences such as temperature and humidity cannot be directly considered in the numerical simulation, but their effect is taken into account in the material parameters.

This section is divided into three parts. In the first part, the numerical simulation setup is presented, including the construction of morphological models, the establishment of boundary conditions, and the determination of material parameters. The second part focuses on the fracture evolution in the FPZ. Finally, the impact of aggregate size is discussed at the end of this section.

5.1. Numerical simulation setups

This section is focused on constructing numerical models that can be compared to the experiments in Otsuka and Date (2000) in terms of dimensions, boundary conditions, morphological structure, and material properties. It is presented in the following parts how we attain this purpose.

5.1.1. Dimensions and boundary conditions of the specimen

The dimensions of the specimen in experiments are given in Fig. 6(a). It is a notched specimen that is made from a cubic plate. In experiments, the specimen is loaded in tension under displacement control through two steel plates bonded to the specimen using an adhesive. To match the experimental setup, the boundary conditions of the numerical simulation are also set in the same manner, as shown in Fig. 6(b).

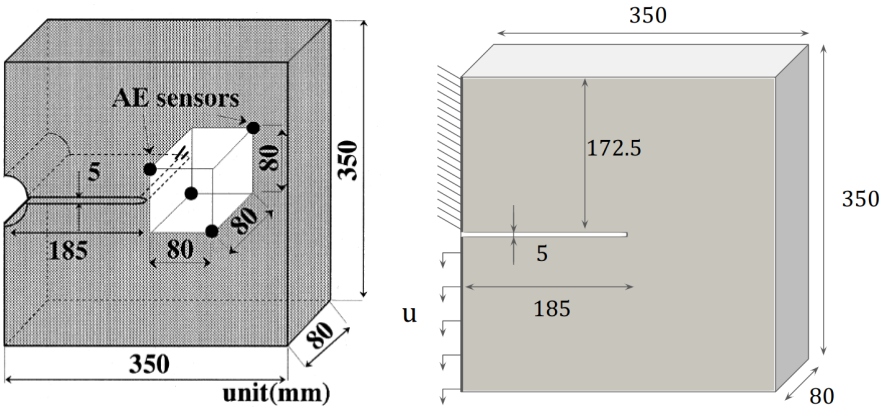

(a) Experimental specimen geometry (b) Numerical specimen geometry

Figure 6: Geometry information of the notched cube specimen in experiments (Otsuka and Date, 2000) and in simulations.

5.1.2. Construction of the morphological models

Given that the dimensions of the numerical specimen have now been defined, the next step is to construct the morphological heterogeneity model. In this paper, the specimen heterogeneity is taken into account by considering two material phases: matrix and aggregates. The tool used to construct the heterogeneity structure is the sphere packing method, as described in (Stamati, Andò, Roubin, Cailletaud, Wiebicke, Pinzon, Couture, Hurley, Caulk, Caillerie et al., 2020). The key point is to generate N spheres of different diameters ($[d_{min}, d_{max}]$) and then arrange them randomly in the field while ensuring a minimum rejection length between them to avoid overlaps.

In experiments, three types of concretes are investigated, which are distinguished by their maximum aggregate size d_{max}: 10, 15, and 20 millimeters. However, there is no information available on the volume fraction and granularity curves of the aggregates. Hence, in the numerical simulations of this section, a volume fraction of 30% is chosen for all three types of concrete, and an 'S-shaped' curve is assumed for the granulometry curve to approximate a general situation in concrete. The minimum aggregate size for all three types of concrete is selected as 5 millimeters to eliminate any differences between them.

Within a range of sphere diameters $[d_{min}, d_{max}]$, the size distribution of the spheres is nearly linear. Therefore, to construct the 'S'-shaped granulometry curves, six classes of spheres are used, as shown in Table. 1.

Table 1
Diameter ranging ([mm]) for three different d_{max} concretes. Six classes are used to reproduce the "S" shaped granulometry curve.

Class	d_{max} = 10 mm	d_{max} = 15 mm	d_{max} = 20 mm	Relative percentage
1	[5.0, 5.83]	[5.0,6.67]	[5.0,7.5]	4%
2	[5.83, 6.67]	[6.67, 8.33]	[7.5, 10.0]	17%
3	[6.67, 7.5]	[8.33, 10.0]	[10.0, 12.5]	29%
4	[7.5, 8.33]	[10.0, 11.67]	[12.5, 15.0]	29%
5	[8.33, 9.17]	[11.67, 13.33]	[15.0, 17.5]	17%
6	[9.17, 10.0]	[13.33, 15.0]	[17.5, 20.0]	4%

As previously stated, the spheres are randomly arranged in the field, which can result in differences between generations, even with the same settings. The size of the statistical sample is not large enough to reduce this numerical discrepancy. Therefore, this section generates six different fields (noted as r1, r2, r3, r4, r5, and r6) for each type of concrete. The measured granulometry curves are displayed in Fig. 7. It can be seen that there is no obvious difference between the six generations by applying the same setting.

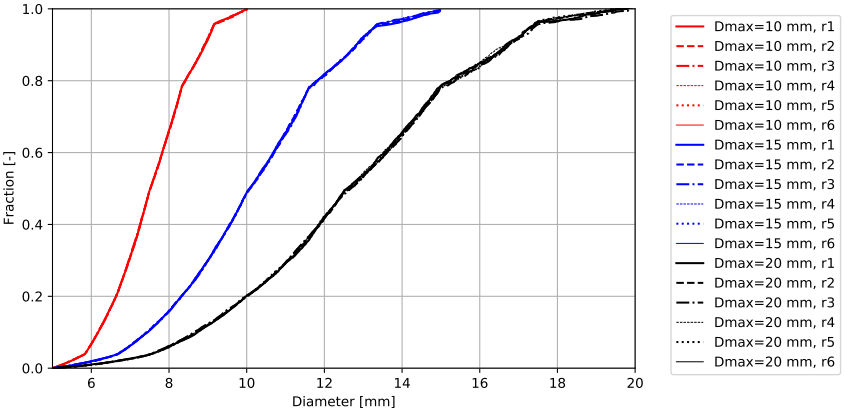

Figure 7: Measured granulometry curves for each type of concrete.

It is worth noting that in the E-FEM model of this paper, only one weak discontinuity is embedded in the finite element. Therefore, a finite element can only correctly present morphological information if at most one heterogeneity

interface passes through the element. To meet this requirement, the size of the finite element must be smaller than the minimum distance between each sphere. However, the small aggregates and the narrowness between spheres will increase the fin finite element mesh requirement, which will significantly boost the computational time and memory. Therefore, the choice is made to simulate the specimen in two parts: a coarse part and a refined part (see Fig.8). The projection of the morphological structure to the mesh is shown in Fig. 9.

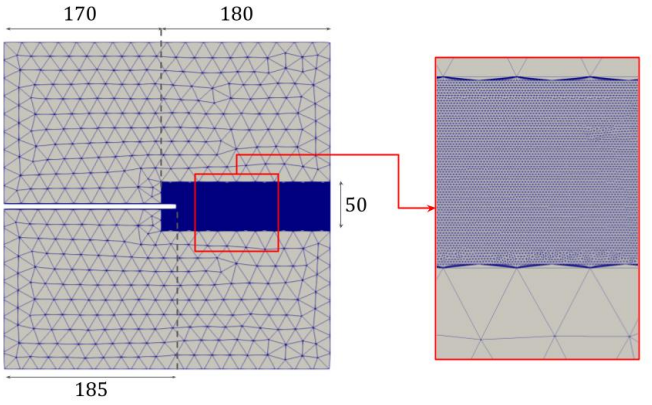

Figure 8: Basic geometry information about the mesh with a zoomed view at the refined zone.

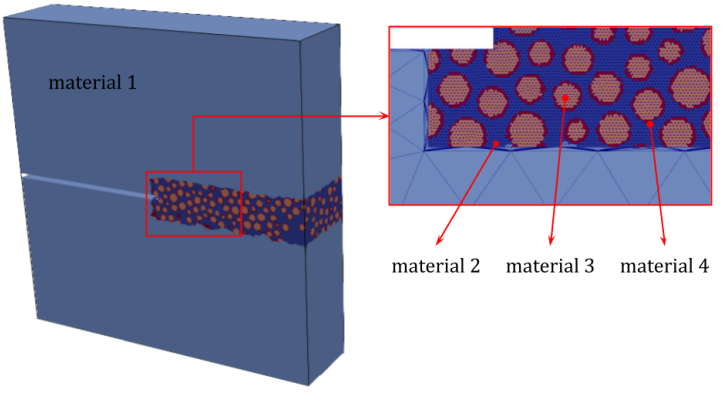

Figure 9: Projection of the defined field with random morphology to an unstructured mesh.

The coarse mesh part, as shown in Fig. 8, has an average finite element size of 20 mm. It is a homogenized zone, which is considered as a merged homogeneous material of the cement paste and the aggregates. The homogeneous material (note as material 1, see Fig. 9) is considered to be purely elastic based on the fact that the most significant crack pattern is mainly observed in the notched part of the specimen.

The refined part, on the other hand, has an average finished element size of 0.9 mm. It is a heterogeneous area that is composed of cement paste and aggregates. After the projection, three types of elements are generated: material 2 represents the cement paste which contains cement and river sands; material 3 represents the aggregates; and material 4 represents the weakly enhanced elements which carries the geometry information about the heterogeneity interface. It can be seen from Fig. 9 that the weakly enhanced element of one aggregate does not overlap another weakly enhanced element of another aggregate. The fracture behaviors of the specimen occur only in the refined region. The crack pattern is one of the most important points in this section.

For further information, the morphological model comprises approximately 870 thousand nodes and 5.4 million elements, requiring approximately 6 GB of computing memory. As previously stated, the differences between genera-

tions are a result of the randomly generated morphological structures, such as the positions of the aggregates. Therefore, to avoid falling into particular cases, six different fields are generated for the three types of concretes (d_{max} = 10 mm, 15 mm, and 20 mm).

5.1.3. Identification of material parameters

The material parameters at the meso-scale are determined by conducting an inverse analysis, which involves minimizing the discrepancy between the numerical results, which is the average response of three generations, and the experimental results. This process enables the identification of four parameters for each type of element: Young's module E, Poisson's ratio ν, critical tensile strength σ_y, and the fracture energy $\mathcal{G}_{op}$. The former two parameters are elastic parameters and can be defined by comparing numerical and experimental results in the elastic phase. The latter two parameters are critical parameters, which are related to the failure behaviors of the concrete. The load curve in terms of the crack opening displacement (COD) is plotted in Fig. 10, in which, the maximum aggregate size of concrete is 10 mm.

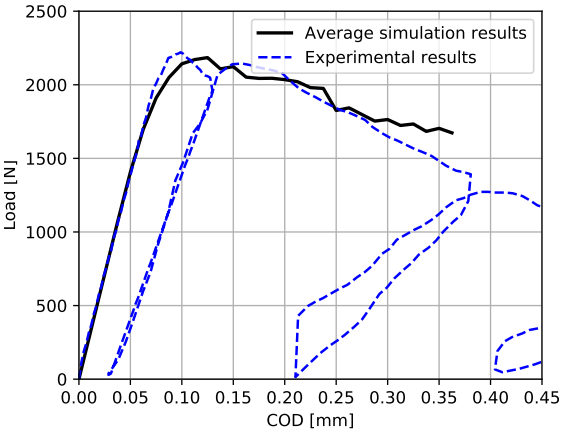

Figure 10: Experiment (Otsuka and Date, 2000) and simulation load curve of d_{max} = 10 mm concrete in terms of the crack opening displacement (COD).

The parameter identification process is carried out in three steps.

In the first step, it is assumed that all four types of elements are elastic and have the same parameters as material 1, the homogenized material of the cement paste and aggregates. The purpose of this step is to determine the elastic parameters of material 1, as it is considered to be purely elastic and therefore has no critical parameters to be identified.

In the second step, the elastic parameters of the materials in the refined zone are determined. It is assumed that materials 2, 3, and 4 are purely elastic. Firstly, the Young's modulus and the Poisson's coefficient of the aggregates are selected. Based on the research of Makani (Makani, 2014), the Young's modulus of the calcium type aggregates of concrete (material 3) is chosen to be 70 GPa, and the Poisson's coefficient is selected to be 0.2. Then, the elastic parameters of the matrix (material 2) can be identified if the numerical simulation reproduces the same macroscopic elastic modulus as the experimental results.

In the final step, the critical parameters of the materials in the refined zone are identified. These parameters, related to the failure behaviors of the concrete at the macro-scale, can be identified if the average numerical simulation produces the same maximum macroscopic resistance and softening curves as the experimental results, see Fig. 10. In this step, the tensile strength of the aggregate is selected based on Makani's research (Makani, 2014), which found that the compressive resistance of calcium aggregates is around 224 MPa. As it is widely known that for geomaterials, the compressive resistance is normally more than 10 times higher than the tensile strength. Therefore, we set the tensile strength of the aggregate at the meso-scale to be 10 MPa.

Considering the two previous steps, the random distribution of aggregates must be taken into account. In this study, we performed these steps on the six independent generations of the d_{max} = 10 mm concrete to obtain an average. Then

the average simulation results are used to be compared with the experimental results. The values of material parameters are iteratively adjusted until the simulation results matched the experimental data as closely as possible.

It is worth noting that our interests are primarily focused on the development and evolution of cracks in the FPZ. To this end, we have decided not to apply the load until the total failure of the material, but to refine the loading steps at the failure initiation stage. In this way, the evolution of the crack pattern in the FPZ at different loading levels can be well captured. The identified parameters for the four types of elements are summaries in Table. 2.

Table 2
Identified parameters of the four types of elements.

Material	E [GPa]	ν [-]	σ_y [MPa]	$\mathcal{G}_{\mathsf{op}}$ [J/m^2]
material 1	6.0	0.2	-	-
material 2	2.2	0.2	2.8	1.2
material 3	70.0	0.2	10.0	1.2
material 4	-	-	2.8	1.0

5.2. Crack pattern - formation of the Fracture Process Zone

Given the identification of the simulation configurations in the previous section, this part focuses on the simulation of the crack pattern in the fracture process zone (FPZ). To illustrate the progression and formation of the FPZ, a concrete sample with $d_{max} = 10$ mm inclusions is selected as an example. Five steps after the maximum resistance are chosen, see Fig. 11.

Fig. 11 presents the front view of our 3D simulation. The aggregates are depicted in a transparent gray color and the cracks are divided into two categories: opening elements and closed elements. The opening elements are displayed in blue and represent elements with continuously increasing crack opening values. The closing elements are displayed in red and correspond to elements with decreasing crack opening values at some point. These two groups of elements are mutually exclusive.

Regarding the opening elements:

- Firstly, we can see from the figure that there is a high density of diffuse micro-cracks surrounding and in front of the macro-crack at each loading stage. Obviously, the orientation and location of these scattered micro-cracks are strongly influenced by the underlying heterogeneous meso-structure.
- Secondly, as the loading increases, some of these micro-cracks eventually transform into macro-cracks, whose path is directly inherited from the micro-cracks at the fine-scale.
- Finally, during macro-crack coalescence, new micro-cracks emerge surrounding and in front of the macro-crack. This transition procedure continues until the complete post-peak failure.

In this work, the transition from micro-cracks to macro-cracks is gradual, and the distinction between the two is based on the size and distribution of cracks. Micro-cracks refer to scattered, separate cracks with relatively small crack opening values, and stresses are still transferred through the interface of the crack. Macro-cracks, on the other hand, are cracks that form the major crack and actually cause the collapse of the material. They are characterized by a relatively large crack opening value, which results in a stress-free crack and crack closures.

In addition to the open elements, the closed elements can also be observed in the figure. As the loading increases, the crack closure behavior takes place mainly in the vicinity and branches of the macro-crackdue to stress release caused by the fully formed macro-crack. Therefore, no closed element can be observed in the area in front of the macro-crack, since there are only spread micro-cracks exist and no macro-crack has formed yet.

The crack features of generations r2 and r3 in the FPZ can be seen in the annex, depicted in Fig. 17 and Fig. 18 respectively. It can be seen that the crack paths of the three generations are all different, due to variations in their meso-structures. However, the pattern of crack evolution for the three generations is consistent. For further information, the simulation result shows several crack features in common with the study of Grassl et al. (2012), such as the tortuous crack path, scattered micro-crack, and the crack closures.

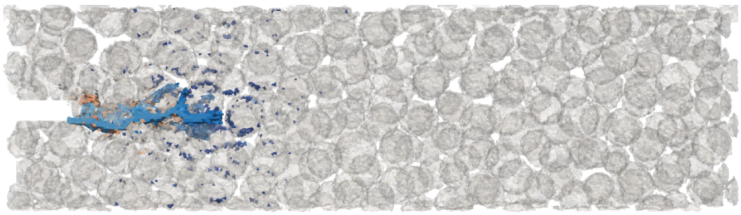

(a) COD = 0.1 mm

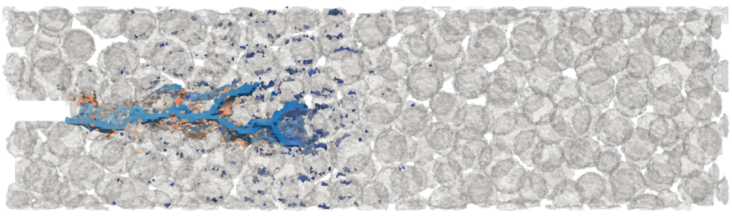

(b) COD = 0.125 mm

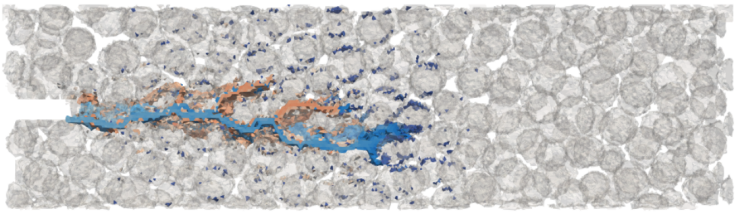

(c) COD = 0.15 mm

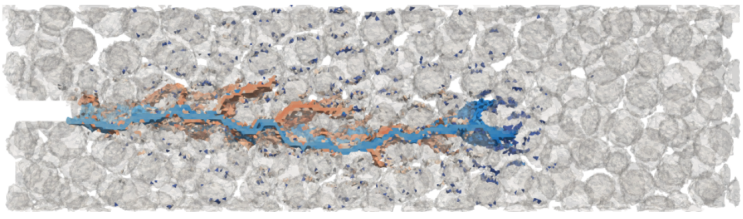

(d) COD = 0.175 mm

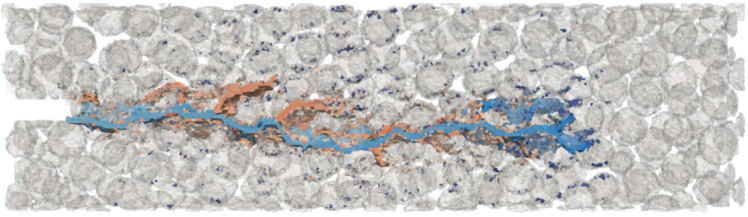

(e) COD = 0.2 mm

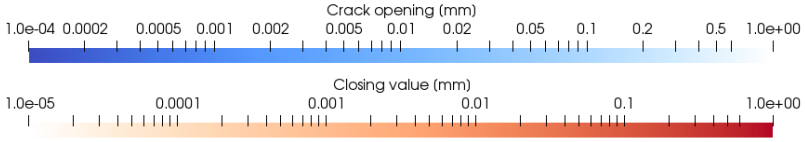

Figure 11: Front view of the crack pattern evolution of d_{max} = 10 mm r1 concrete: crack openings and crack closures (aggregates marked in transparent gray).

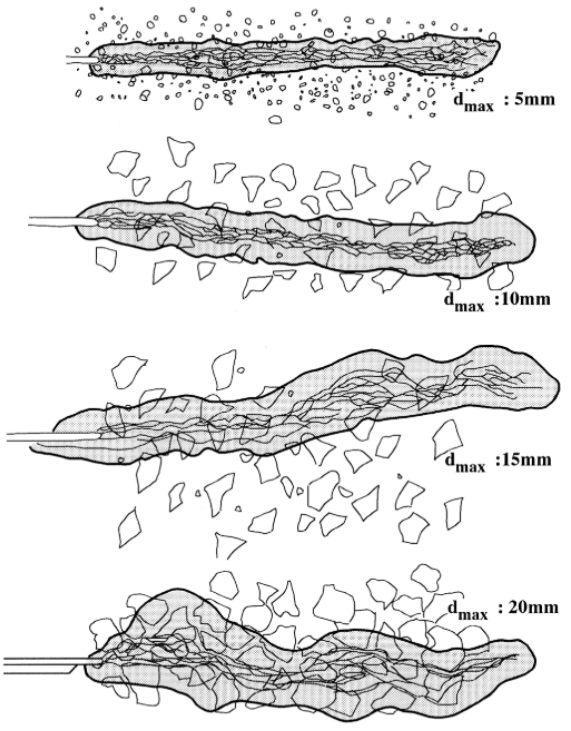

Figure 12: Comparison of FCZ traced from X-ray films of concrete with four different d_{max} (Otsuka and Date, 2000).

5.3. Size effect in the Fracture Process Zone

In this section, the focus is made on the size effect of the inclusions. According to the experimental results in Otsuka and Date (2000), at the peak load, as the maximum inclusion size increases, the width of the Fracture Core Zone (FCZ) increases, while the length of the FCZ decreases, see Fig. 14. Here, the FCZ is defined as the area that carries 70% of the total energy of all AE events, see Fig. 13(a). This size effect can also be observed at the post-peak load, see Fig. 12.

This section contains two parts. The first part of this section examines the relationship between the inclusion size and the dimensions of the FCZ at peak load, and compares the simulation results with the experimental results. The second part focuses on the crack pattern of different d_{max} concrete at post-peak load. A possible explanation of the size effect is given from the numerical point of view.

5.3.1. Effect of the inclusion size at the peak load

In section 5.1.2, three morphological models are constructed for each type of concrete that carrying different d_{max}. In this section, the same material parameters in Table. 2 are applied to these models to investigate the size effect of the inclusions.

To make a reasonable comparison between the experimental results and numerical results, it is necessary to present the method used to measure the dimension of the Fracture Core Zone (FCZ) in the simulations. In experiments, the FCZ is defined as the area carrying 70% of the total energy, as seen in Fig. 13(a). However, it is difficult to define such an area in numerical simulations. Therefore, in this study, the elements in the FCZ are chosen as those that have a crack opening value $[u]$ greater than 0.001 mm. The dimensions of the FCZ are then measured by embedding all these elements in a cuboid and measuring the dimensions of the cuboid, see Fig. 13(b). It is worth noting that isolated elements that located far from other cracks will not be included in the FCZ to prevent overestimation of its length and width. This approach is used for a qualitative comparison between the simulation and experimental results, since a quantitative comparison may lack rigorous validity. The comparison is illustrated in Fig. 14.

Regarding the width of FCZ in experimental results, as shown in Fig. 14(a), there are four experimental tests for

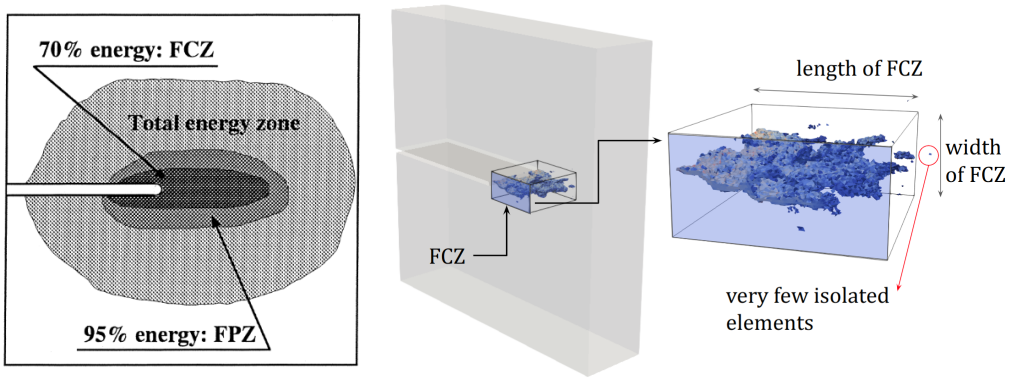

(a) Definition of FCZ and FPZ in experiments (b) Cuboid that envelops elements carrying a crack opening value larger than 0.001 mm

Figure 13: Measurement of the FCZ in experiments (Otsuka and Date, 2000) and in simulations.

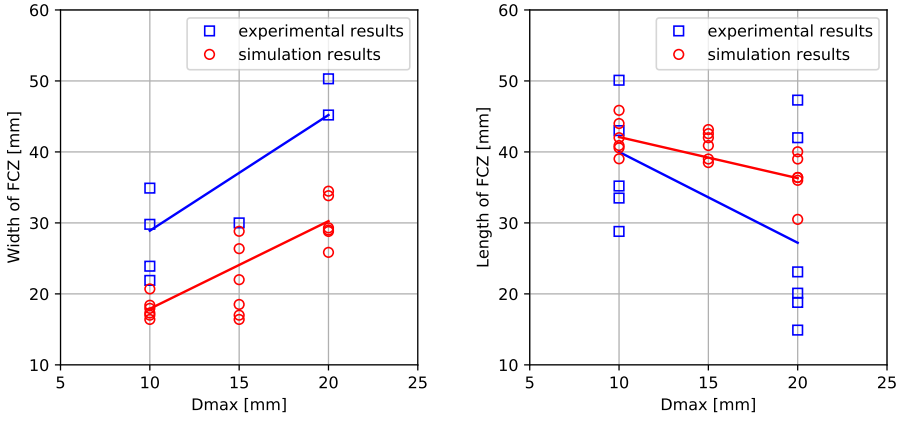

(a) Width of FCZ (b) Length of FCZ

Figure 14: Relationship between d_{max} and dimensions of FCZ at peak load in experiments and in numerical simulations.

inclusion size equal to 10 mm, one test for inclusion size equal to 15 mm, and two tests for inclusion size equal to 20 mm. For the same type of concrete, the maximum discrepancy between two tests of the same concrete can be found at the d_{max} = 10 mm, which is equal to 13.0 mm. The average width increases from 28.9 mm to 45.2 mm as the inclusion size varies from 10 mm to 20 mm. In numerical simulations, there are six simulations for each type of concrete. Similarly, discrepancies can be found between each generation for the same type of concrete, with the maximum difference being 12.42 mm for the d_{max} = 15 mm concrete. The average widths of FCZ are 17.9 mm and 30.25 mm for the smallest and largest inclusion size concrete, respectively.

Regarding the width of FCZ, there are two positive correlations that can be seen between the experimental results and simulation results. Firstly, the average width of the FCZ increases as the maximum inclusion size (d_{max}) increases. Secondly, the discrepancies between two samples of the same type of concrete are observed.

For the former, the increase in the average width of the FCZ with the increase in the maximum inclusion size (d_{max}) is due to the heterogeneous structures in the concrete, as the same material parameters were used for all types of concrete. From the numerical point of view, this effect can be explained by the fact that the cracks are more tortuous as the inclusion size increases, since the cracks tend to deviate through inclusions to avoid obstruction. Readers can refer to the section 5.3.2 for more details. For the latter, clearly, the discrepancy between two samples of the same type of concrete in both experiments and simulations can be explained by the statistical random distribution of aggregates.

Now let us move our attention to the length of FCZ, see Fig. 14(b).

The experimental results of the length of FCZ show that the discrepancies between different samples of the same type of concrete are substantially larger than those in the width of FCZ. The largest difference between two tests is 21.3 mm for the d_{max} = 10 mm concrete and 32.4 mm for the d_{max} = 20 mm concrete. For the d_{max} = 20 mm concrete, the longest FCZ measures 47.3 mm which is three times longer than the shortest FCZ of 14.9 mm. The average length decreases from 40.0 mm to 27.2 mm as the inclusion size increases from 10 mm to 20 mm. As for the simulation results, it can be seen that the average length is larger than it is in experimental results. The discrepancy between tests of the same type of concrete is also smaller.

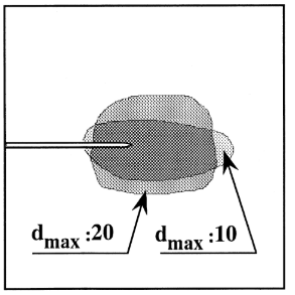

Figure 15: Relationship between d_{max} and dimensions of FCZ at peak load in numerical simulations.

There are two possible reasons for these differences. On the one hand, the number of numerical sample (six samples for each kind of concrete) is insufficient to achieve a statistically meaningful conclusion. On the other hand, the length of FCZ in numerical simulations may be affected by the choose of our morphological model. It is presented in Section. 5.1.2 that the numerical sample is divided into two parts, an elastic part and a heterogeneous part. The failure behaviors can only appear at the latter part. Limited by the computation power, the width of this region is chosen to be 50 mm. It is can be noticed in Fig. 11 that the farthest micro-cracks can be observed up to the border of the refined zone, which indicates that the refined zone is obviously insufficient to capture all fracture behaviors in the FPZ. This may lead to a longer FCZ since there is no energy being dissipated outside the 50 mm refined zone, which is not consistent to the experimental observation in Fig. 15. Moreover, This effect is more pronounced for concrete with larger aggregates, as the FCZ of large d_{max} concrete is shorter and wider, and the wider distribution of micro-cracks means reducing the refined zone has a greater impact on the behavior of the FCZ.

5.3.2. Effect of the inclusion size at the post-peak load

In this part, we focus on the crack pattern of the different d_{max} concretes at the post-peak load. The crack pattern of three types of concrete is plotted in Fig. 16. It can be seen that they share many patterns in common, such as the diffused micro-cracks besides and in front of the macro-crack, branching besides the macro-crack, and the closed elements at the branches and neighboring parts of the macro-crack.

Most importantly, it can also be seen from the figure that as the d_{max} increases, the macro-crack becomes more circuitous. It is due to the fact that in case of being obstructed by an inclusion, the crack tend to deviate to continue propagating. Therefore, larger inclusions lead to a more tortuous crack pattern and underlying more dissipated energy in the crack path. Hence, larger inclusion size would lead to a wider and shorter FCZ. It could be a possible explanation for the size effect from the numerical point of view.

6. Discussions and conclusions

This paper uses a meso-scale approach to model the Fracture Process Zone (FPZ) in concrete. Several notched cube specimens with statistical random distributed aggregates were performed to investigate the formation of the FPZ and its relationship with the inclusion size, namely, the size effect.

At the meso-scale, the specimen is considered as a highly heterogeneous material, and the evolution crack pattern from the fine-scale spread micro-cracks to macro-cracks can be observed. Here, the aggregates are performed explicitly by the sphere packing method (Stamati et al., 2020) and the embedded weak discontinuities (Ortiz et al., 1987; Sukumar et al., 2001). The cracks are depicted by the strong discontinuities (Simo et al., 1993; Wells, 2001). Providing that the

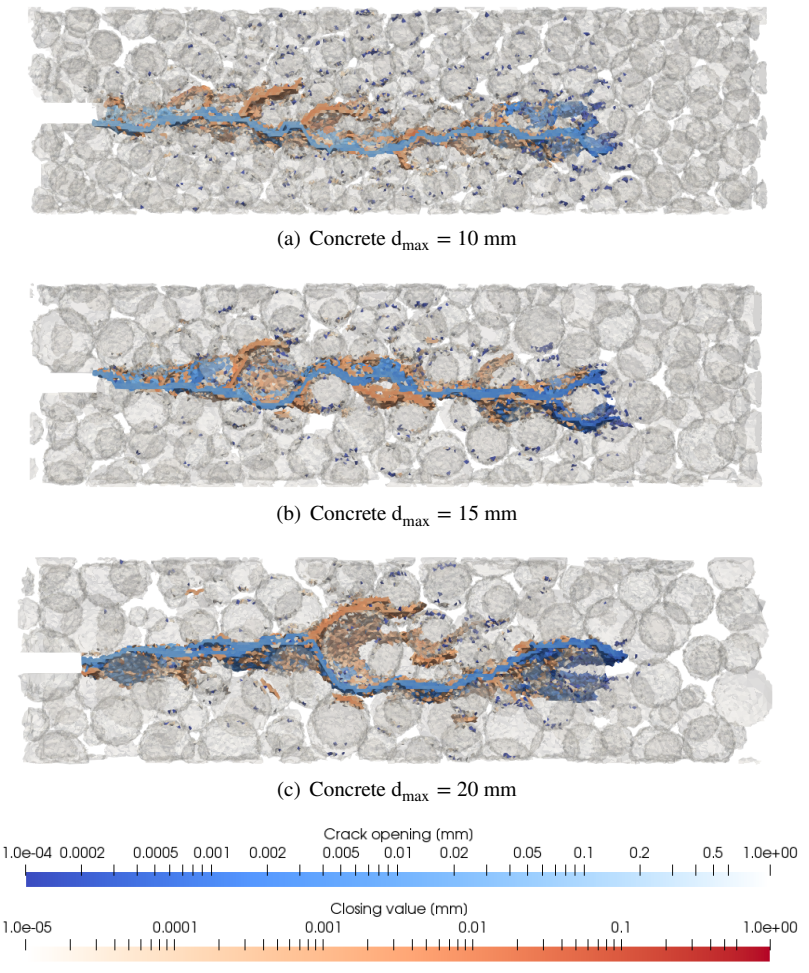

(a) Concrete d_{max} = 10 mm

(b) Concrete d_{max} = 15 mm

(c) Concrete d_{max} = 20 mm

Figure 16: Relationships between Dmax and dimension of the FCZ at peak load (Otsuka and Date, 2000).

mode-I crack mode is fairly a common choice for the modeling of FPZ, a crack opening-closing E-FEM model (Sun et al., 2021) is applied in this paper. By combining the weak/strong enhancements, the presented E-FEM model is capable of simulating complex crack pattern evolution and considering the interaction between cracks and aggregates.

The numerical simulations are compared with relevant experiments that is realized by Otsuka and Date (2000). The comparison results in several conclusions:

- First, the failure process in the FPZ is a complex procedure starting from the diffused local micro-cracks whose location and orientation are closely related to the heterogeneity structure. The coalescence of micro-cracks forms macro-cracks, while new micro-cracks appear in the front of the macro-crack. Meanwhile, crack closures can be observed at the stress release zone, such as at the branches of the major macro-crack.

- Second, we managed to simulate the experimentally observed size effect, that as the inclusion size increases, the FCZ becomes wider and shorter. The most likely explanation for this observation is that a larger inclusion size leads to more tortuous cracks. It is because the crack tends to deviate through inclusions to avoid obstruction. Thus more circuitous cracks would lead to more energy being dissipated in the crack path.

However, being limited by the computation power, the number of numerical samples is insufficient to achieve a statistically meaningful conclusion. Because of the same limitation, the non-linear zone (zone carrying refined meshes) is chosen to have a width of 50 mm, which is not enough to capture all local-scale cracks in the notched cube specimen. It could be a possible reason that addresses the difference between the simulation and experiments in the comparison of the FCZ length.

Notwithstanding these limitations, the study certainly adds to our understanding of the crack evolution inside the FPZ and its relationship with the material composite structure. Further research in this field would be of great help in increasing calculating efficiency and reducing required computation power.

References

Barenblatt, G.I., 1962. The mathematical theory of equilibrium cracks in brittle fracture, in: Advances in applied mechanics. Elsevier. volume 7, pp. 55–129.

Bažant, Z.P., Jirásek, M., 2002. Nonlocal integral formulations of plasticity and damage: survey of progress. Journal of engineering mechanics 128, 1119–1149.

Bažant, Z.P., Oh, B.H., 1983. Crack band theory for fracture of concrete. Matériaux et construction 16, 155–177.

Bažant, Z.P., Pijaudier-Cabot, G., 1989. Measurement of characteristic length of nonlocal continuum. Journal of Engineering Mechanics 115, 755–767.

Benkemoun, N., Hautefeuille, M., Colliat, J., Ibrahimbegovic, A., . Heterogeneous materials failure: 3d meso-scale modeling with embedded discontinuities .

Benkemoun, N., Hautefeuille, M., Colliat, J.B., Ibrahimbegovic, A., 2010. Failure of heterogeneous materials: 3d meso-scale fe models with embedded discontinuities. International journal for numerical methods in engineering 82, 1671–1688.

Benvenuti, E., Tralli, A., 2012. Simulation of finite-width process zone in concrete-like materials by means of a regularized extended finite element model. Computational Mechanics 50, 479–497.

Brancherie, D., Ibrahimbegovic, A., 2009. Novel anisotropic continuum-discrete damage model capable of representing localized failure of massive structures: Part i: theoretical formulation and numerical implementation. Engineering Computations: Int J for Computer-Aided Engineering 26, 100–127.

Choi, S., Shah, S., 1997. Measurement of deformations on concrete subjected to compression using image correlation. Experimental mechanics 37, 307–313.

Corless, R.M., Gonnet, G.H., Hare, D.E., Jeffrey, D.J., Knuth, D.E., 1996. On the lambertw function. Advances in Computational mathematics 5, 329–359.

Corr, D., Accardi, M., Graham-Brady, L., Shah, S., 2007. Digital image correlation analysis of interfacial debonding properties and fracture behavior in concrete. Engineering Fracture Mechanics 74, 109–121.

Dias-da Costa, D., Alfaiate, J., Sluys, L., Júlio, E., 2009a. A discrete strong discontinuity approach. Engineering Fracture Mechanics 76, 1176–1201.

Dias-da Costa, D., Alfaiate, J., Sluys, L., Júlio, E., 2009b. Towards a generalization of a discrete strong discontinuity approach. Computer Methods in Applied Mechanics and Engineering 198, 3670–3681.

Dugdale, D.S., 1960. Yielding of steel sheets containing slits. Journal of the Mechanics and Physics of Solids 8, 100–104.

Dvorkin, E.N., Cuitiño, A.M., Gioia, G., 1990. Finite elements with displacement interpolated embedded localization lines insensitive to mesh size and distortions. International journal for numerical methods in engineering 30, 541–564.

Eliáš, J., Vořechovskỳ, M., Skoček, J., Bažant, Z.P., 2015. Stochastic discrete meso-scale simulations of concrete fracture: Comparison to experimental data. Engineering fracture mechanics 135, 1–16.

Georgioudakis, M., Stefanou, G., Papadrakakis, M., 2014. Stochastic failure analysis of structures with softening materials. Engineering Structures 61, 13–21.

Grassl, P., Bažant, Z.P., 2009. Random lattice-particle simulation of statistical size effect in quasi-brittle structures failing at crack initiation. Journal of engineering mechanics 135, 85–92.

Grassl, P., Grégoire, D., Solano, L.R., Pijaudier-Cabot, G., 2012. Meso-scale modelling of the size effect on the fracture process zone of concrete. International Journal of Solids and Structures 49, 1818–1827.

Grassl, P., Jirásek, M., 2010. Meso-scale approach to modelling the fracture process zone of concrete subjected to uniaxial tension. International Journal of Solids and Structures 47, 957–968.

Griffith, A.A., 1921. Vi. the phenomena of rupture and flow in solids. Philosophical transactions of the royal society of london. Series A, containing papers of a mathematical or physical character 221, 163–198.

Gurtin, M.E., 1973. The linear theory of elasticity, in: Linear theories of elasticity and thermoelasticity. Springer, pp. 1–295.

Haidar, K., Pijaudier-Cabot, G., Dubé, J.F., Loukili, A., 2005. Correlation between the internal length, the fracture process zone and size effect in model materials. Materials and structures 38, 201–210.

Hauseux, P., Roubin, E., Seyedi, D.M., Colliat, J.B., 2016. Fe modelling with strong discontinuities for 3d tensile and shear fractures: application to underground excavation. Computer Methods in Applied Mechanics and Engineering 309, 269–287.

Hillerborg, A., Modéer, M., Petersson, P.E., 1976. Analysis of crack formation and crack growth in concrete by means of fracture mechanics and finite elements. Cement and concrete research 6, 773–781.

Huang, Y., Yang, Z., Ren, W., Liu, G., Zhang, C., 2015. 3d meso-scale fracture modelling and validation of concrete based on in-situ x-ray computed tomography images using damage plasticity model. International Journal of Solids and Structures 67, 340–352.

Ibrahimbegović, A., Markovič, D., 2003. Strong coupling methods in multi-phase and multi-scale modeling of inelastic behavior of heterogeneous structures. Computer methods in applied mechanics and engineering 192, 3089–3107.

Ibrahimbegovic, A., Melnyk, S., 2007. Embedded discontinuity finite element method for modeling of localized failure in heterogeneous materials with structured mesh: an alternative to extended finite element method. Computational Mechanics 40, 149–155.

Jebli, M., Jamin, F., Malachanne, E., Garcia-Diaz, E., El Youssoufi, M.S., 2018. Experimental characterization of mechanical properties of the cement-aggregate interface in concrete. Construction and Building Materials 161, 16–25.

Kamel, K.E.M., Colliat, J.B., Gerard, P., Massart, T.J., 2020. Comparison of advanced discretization techniques for image-based modelling of heterogeneous porous rocks. Acta Geotechnica 15, 57–77.

Kucerova, A., Brancherie, D., Ibrahimbegovic, A., Zeman, J., Bittnar, Z., 2009. Novel anisotropic continuum-discrete damage model capable of representing localized failure of massive structures: Part ii: identification from tests under heterogeneous stress field. Engineering Computations: Int J for Computer-Aided Engineering 26, 128–144.

Kumar, M., Singh, I., Mishra, B., Ahmad, S., Rao, A.V., Kumar, V., 2018. Mixed mode crack growth in elasto-plastic-creeping solids using xfem. Engineering fracture mechanics 199, 489–517.

Laborin, A.O., Malecot, Y., Roubin, E., Daudeville, L., . Modelling of triaxial fracture processes in heterogeneous quasi-brittle materials using the embedded finite element method (e-fem) .

Landis, E.N., 1999. Micro–macro fracture relationships and acoustic emissions in concrete. Construction and Building Materials 13, 65–72.

Landis, E.N., Nagy, E.N., Keane, D.T., 2003. Microstructure and fracture in three dimensions. Engineering Fracture Mechanics 70, 911–925.

Li, S., Abdel-Wahab, A., Demirci, E., Silberschmidt, V.V., 2014. Fracture process in cortical bone: X-fem analysis of microstructured models, in: Fracture Phenomena in Nature and Technology. Springer, pp. 43–55.

Luković, M., Šavija, B., Schlangen, E., Ye, G., Van Breugel, K., 2016. A 3d lattice modelling study of drying shrinkage damage in concrete repair systems. Materials 9, 575.

Makani, A., 2014. Analytical estimate of the mechanical behavior of rock: Granitic aggregates. Arabian Journal for Science and Engineering 39, 3651–3663.

Matthies, H., Strang, G., 1979. The solution of nonlinear finite element equations. International journal for numerical methods in engineering 14, 1613–1626.

Mihashi, H., Nomura, N., 1996. Correlation between characteristics of fracture process zone and tension-softening properties of concrete. Nuclear engineering and design 165, 359–376.

Moës, N., Belytschko, T., 2002. Extended finite element method for cohesive crack growth. Engineering fracture mechanics 69, 813–833.

Moës, N., Cloirec, M., Cartraud, P., Remacle, J.F., 2003. A computational approach to handle complex microstructure geometries. Computer methods in applied mechanics and engineering 192, 3163–3177.

Moës, N., Dolbow, J., Belytschko, T., 1999. A finite element method for crack growth without remeshing. International journal for numerical methods in engineering 46, 131–150.

Muralidhara, S., Prasad, B.R., Eskandari, H., Karihaloo, B.L., 2010. Fracture process zone size and true fracture energy of concrete using acoustic emission. Construction and Building Materials 24, 479–486.

Nguyen, T.T., Yvonnet, J., Zhu, Q.Z., Bornert, M., Chateau, C., 2015. A phase field method to simulate crack nucleation and propagation in strongly heterogeneous materials from direct imaging of their microstructure. Engineering Fracture Mechanics 139, 18–39.

Nitka, M., Tejchman, J., et al., 2015. Modelling of concrete fracture at aggregate level using fem and dem based on x-ray μct images of internal structure. Engineering fracture mechanics 147, 13–35.

Oliver, J., 1996a. Modelling strong discontinuities in solid mechanics via strain softening constitutive equations. part 1: Fundamentals. International journal for numerical methods in engineering 39, 3575–3600.

Oliver, J., 1996b. Modelling strong discontinuities in solid mechanics via strain softening constitutive equations. part 2: Numerical simulation. International journal for numerical methods in engineering 39, 3575–3600.

Oliver, J., 2000. On the discrete constitutive models induced by strong discontinuity kinematics and continuum constitutive equations. International journal of solids and structures 37, 7207–7229.

Ortiz, M., Leroy, Y., Needleman, A., 1987. A finite element method for localized failure analysis. Computer methods in applied mechanics and engineering 61, 189–214.

Otsuka, K., Date, H., 2000. Fracture process zone in concrete tension specimen. Engineering Fracture Mechanics 65, 111–131.

Pan, Y., Prado, A., Porras, R., Hafez, O.M., Bolander, J.E., 2017. Lattice modeling of early-age behavior of structural concrete. Materials 10, 231.

Pan, Z., Ma, R., Wang, D., Chen, A., 2018. A review of lattice type model in fracture mechanics: theory, applications, and perspectives. Engineering Fracture Mechanics 190, 382–409.

Rice, J.R., 1968. A path independent integral and the approximate analysis of strain concentration by notches and cracks .

Rice, J.R., et al., 1968. Mathematical analysis in the mechanics of fracture. Fracture: an advanced treatise 2, 191–311.

Rodrigues, E.A., Manzoli, O.L., Bitencourt Jr, L.A., 2020. 3d concurrent multiscale model for crack propagation in concrete. Computer Methods in Applied Mechanics and Engineering 361, 112813.

Roubin, E., Vallade, A., Benkemoun, N., Colliat, J.B., 2015. Multi-scale failure of heterogeneous materials: A double kinematics enhancement for embedded finite element method. International Journal of Solids and Structures 52, 180–196.

Scrivener, K.L., Crumbie, A.K., Laugesen, P., 2004. The interfacial transition zone (itz) between cement paste and aggregate in concrete. Interface science 12, 411–421.

Simo, J., Oliver, J., 1994. A new approach to the analysis and simulation of strain softening in solids. Fracture and damage in quasibrittle structures , 25–39.

Simo, J.C., Oliver, J., Armero, F., 1993. An analysis of strong discontinuities induced by strain-softening in rate-independent inelastic solids. Computational mechanics 12, 277–296.

Stamati, O., Andò, E., Roubin, E., Cailletaud, R., Wiebicke, M., Pinzon, G., Couture, C., Hurley, R.C., Caulk, R., Caillerie, D., et al., 2020. spam: Software for practical analysis of materials. Journal of Open Source Software 5, 2286.

Sukumar, N., Chopp, D.L., Moës, N., Belytschko, T., 2001. Modeling holes and inclusions by level sets in the extended finite-element method. Computer methods in applied mechanics and engineering 190, 6183–6200.

Sun, Y., Roubin, E., Shao, J., Colliat, J.B., 2021. Strong discontinuity fe analysis for heterogeneous materials: The role of crack closure mechanism. Computers & Structures 251, 106556.

Taylor, R.L., 1987. FEAP-ein finite element analysis programm. Ing.-Gemeinschaft Klee & Wrigges.

Tejchman, J., et al., 2010. Calculations of fracture process zones on meso-scale in notched concrete beams subjected to three-point bending. European Journal of Mechanics-A/Solids 29, 746–760.

Tijssens, M.G., Sluys, B.L., van der Giessen, E., 2000. Numerical simulation of quasi-brittle fracture using damaging cohesive surfaces. European Journal of Mechanics-A/Solids 19, 761–779.
Trawiński, W., Tejchman, J., Bobiński, J., 2018. A three-dimensional meso-scale modelling of concrete fracture, based on cohesive elements and x-ray μct images. Engineering fracture mechanics 189, 27–50.
Veselỳ, V., Frantík, P., 2014. An application for the fracture characterisation of quasi-brittle materials taking into account fracture process zone influence. Advances in Engineering Software 72, 66–76.
Vořechovskỳ, M., Sadílek, V., 2008. Computational modeling of size effects in concrete specimens under uniaxial tension. International journal of fracture 154, 27–49.
Wells, A., 1961. Crack propagation symposium proceedings. Cranfield College of Aeronautics 1, 210.
Wells, G.N., 2001. Discontinuous modelling of strain localisation and failure. Ph.D. thesis.
Wilson, E.L., 1974. The static condensation algorithm. International Journal for Numerical Methods in Engineering 8, 198–203.
Wittmann, F.H., Hu, X., 1991. Fracture process zone in cementitious materials. International Journal of Fracture 51, 3–18.
Wu, Z., Rong, H., Zheng, J., Xu, F., Dong, W., 2011. An experimental investigation on the fpz properties in concrete using digital image correlation technique. Engineering Fracture Mechanics 78, 2978–2990.
Xenos, D., Grégoire, D., Morel, S., Grassl, P., 2015. Calibration of nonlocal models for tensile fracture in quasi-brittle heterogeneous materials. Journal of the Mechanics and Physics of Solids 82, 48–60.
Yue, S., Roubin, E., Jianfu, S., Colliat, J.B., 2021. Fe modeling of concrete with strong discontinuities for 3d shear fractures and comparison with experimental results. Engineering Fracture Mechanics , 107752.
Zhang, Y., Chen, Q., Wang, Z., Zhang, J., Wang, Z., Li, Z., 2019. 3d mesoscale fracture analysis of concrete under complex loading. Engineering Fracture Mechanics 220, 106646.
Zhou, F., Molinari, J.F., 2004. Dynamic crack propagation with cohesive elements: a methodology to address mesh dependency. International Journal for Numerical Methods in Engineering 59, 1–24.
Zhou, R., Chen, H.M., 2019. Mesoscopic investigation of size effect in notched concrete beams: The role of fracture process zone. Engineering Fracture Mechanics 212, 136–152.
Zhou, R., Song, Z., Lu, Y., 2017. 3d mesoscale finite element modelling of concrete. Computers & Structures 192, 96–113.

Appendix A - Expressions of the matrix

The explicit expressions of the matrix in Eq. 11 and Eq. 12 are listed in this appendix.

$$\boldsymbol{K}_{\mathrm{bb}} = \boldsymbol{B}^T \left(V^+ \boldsymbol{C}^+ + V^- \boldsymbol{C}^- \right) \boldsymbol{B}$$

$$\boldsymbol{K}_{\mathrm{bw}} = \frac{V^+ V^-}{V} \boldsymbol{B}^T (\boldsymbol{C}^+ - \boldsymbol{C}^-) \boldsymbol{H}_{\mathrm{w}}$$

$$\boldsymbol{K}_{\mathrm{bs}} = \boldsymbol{B}^T (V^+ \boldsymbol{C}^+ + V^- \boldsymbol{C}^-) \mathbf{G}_{\mathrm{s}} \boldsymbol{n}$$

$$\boldsymbol{K}_{\mathrm{wb}} = \frac{V^+ V^-}{V} \boldsymbol{H}_{\mathrm{w}}{}^T (\boldsymbol{C}^+ - \boldsymbol{C}^-) \boldsymbol{B}$$

$$\boldsymbol{K}_{\mathrm{ww}} = \frac{V^+ V^-}{V} \boldsymbol{H}_{\mathrm{w}}{}^T (V^- \boldsymbol{C}^+ + V^+ \boldsymbol{C}^-) \boldsymbol{H}_{\mathrm{w}}$$

$$\boldsymbol{K}_{\mathrm{ws}} = \frac{V^+ V^-}{V} \boldsymbol{H}_{\mathrm{w}} (\boldsymbol{C}^+ - \boldsymbol{C}^-) \mathbf{G}_{\mathrm{s}} \boldsymbol{n}.$$

$$\boldsymbol{K}_{\mathrm{s^*b}} = \frac{\partial \sigma_{\mathrm{eq}}}{\partial \boldsymbol{T}} \frac{1}{V} \boldsymbol{H}_{\mathrm{s}}^{*,T} (V^+ \boldsymbol{C}^+ + V^- \boldsymbol{C}^-) \boldsymbol{B}$$

$$\boldsymbol{K}_{\mathrm{s^*w}} = \frac{\partial \sigma_{\mathrm{eq}}}{\partial \boldsymbol{T}} \frac{V^+ V^-}{V} \boldsymbol{H}_{\mathrm{s}}^{*,T} (\boldsymbol{C}^+ - \boldsymbol{C}^-) \boldsymbol{H}_{\mathrm{w}}$$

$$\boldsymbol{K}_{\mathrm{s^*s}} = \frac{\partial \sigma_{\mathrm{eq}}}{\partial \boldsymbol{T}} \frac{1}{V} \boldsymbol{H}_{\mathrm{s}}^{*,T} (V^+ \boldsymbol{C}^+ + V^- \boldsymbol{C}^-) \mathbf{G}_{\mathrm{s}} \boldsymbol{n}$$

$$K_{\mathrm{qo}} = \frac{\sigma_y^2}{\mathcal{G}_{\mathrm{op}}} e^{-\sigma_{\mathrm{y}}[u]/\mathcal{G}_{\mathrm{op}}}$$

$$K_{\mathrm{qc}} = \frac{\mathcal{G}_{\mathrm{cl}}}{[u]_{\max}[u]}$$

The definition of each term in the expressions is given as:

- $\boldsymbol{B}$: standard strain interpolation matrix
- $V, V^+/V^-$: volume of the element, volume of the upper/lower part of the element

- C^+/C^-: elastic stiffness matrix of the upper/lower part of the element
- $\boldsymbol{H}_{\mathrm{w}}$: equivalent normal vector matrix
- $\mathbf{G}_{\mathrm{s}}$: strong enhanced strain interpolation matrix of the actual field
- $\boldsymbol{n}$: normal vector of the discontinuity interface
- $\boldsymbol{H}_{\mathrm{s}}^{*}$: Voigt form of the normal vector that can be calculated by $(\bullet \otimes \boldsymbol{n})^{\mathrm{sym}}$
- $[|\boldsymbol{u}|]$: jump in the displacement field
- $[u]_{\mathrm{max}}$: maximum crack opening value of an element

Readers can refer to Roubin et al. (2015); Yue et al. (2021); Sun et al. (2021) for details of developments.

Appendix B - Crack evolution of two other generations of $\mathbf{d_{max}} = 10$ mm concrete

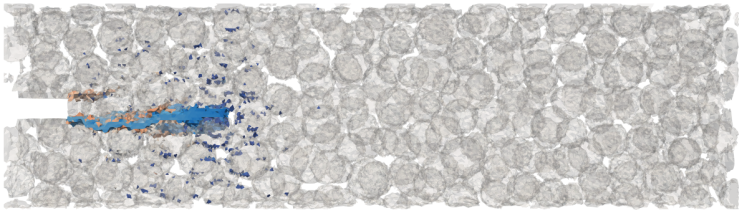

(a) COD = 0.1 mm

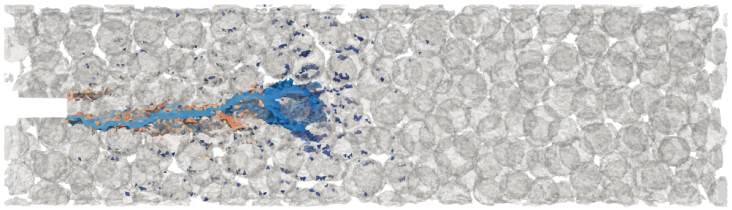

(b) COD = 0.125 mm

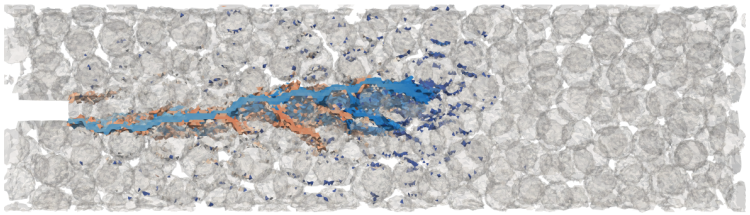

(c) COD = 0.15 mm

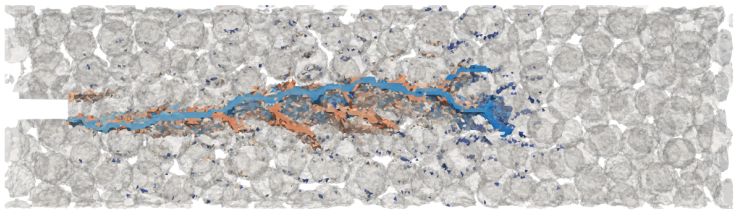

(d) COD = 0.175 mm

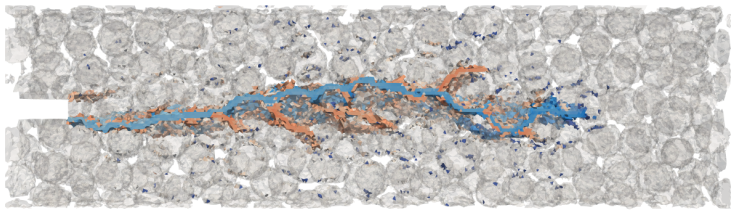

(e) COD = 0.2 mm

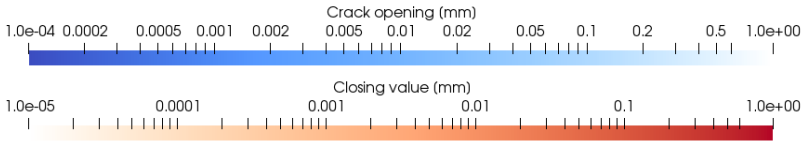

Figure 17: Crack pattern evolution of d_{max} = 10 mm r2 concrete: crack openings and crack closures.

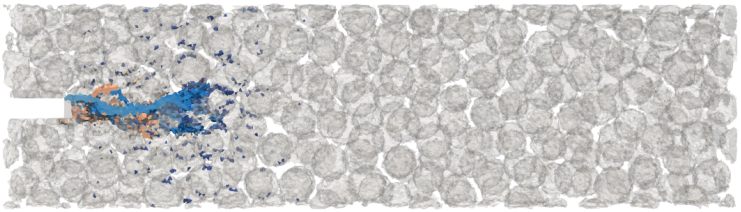

(a) COD = 0.1 mm

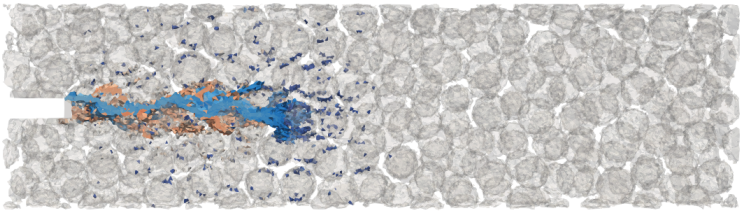

(b) COD = 0.125 mm

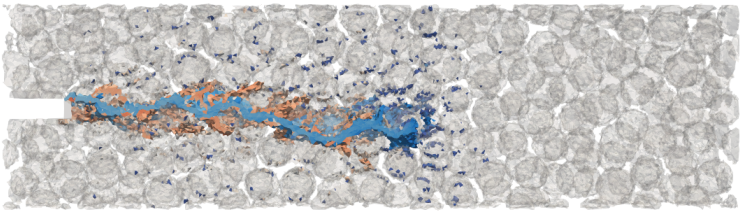

(c) COD = 0.15 mm

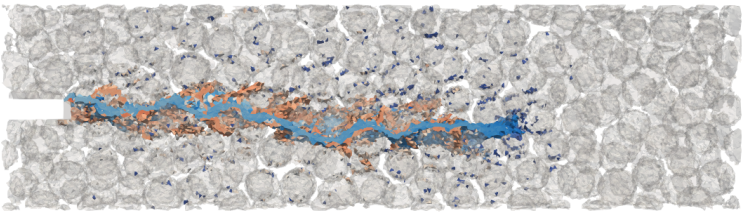

(d) COD = 0.175 mm

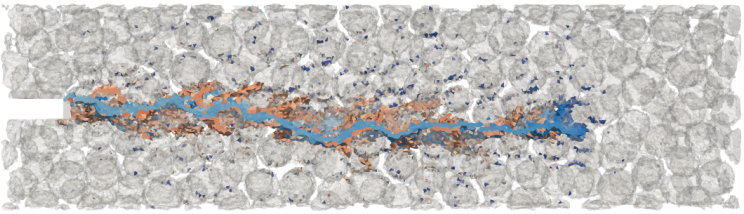

(e) COD = 0.2 mm

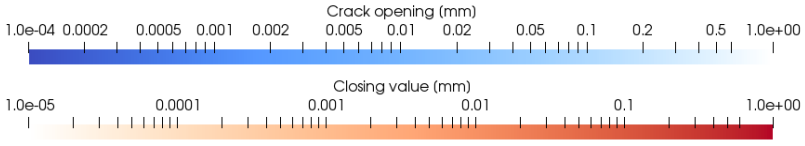

Figure 18: Crack pattern evolution of d_{max} = 10 mm r3 concrete: crack openings and crack closures.